

Single Crystal to Polycrystal Neutron Transmission Simulation

L.L. Dessieux,^{1,2, a)} A.D. Stoica,^{2, b)} and P.R. Bingham^{2, c)}¹⁾Physics Department, University of Tennessee Knoxville, USA²⁾Oak Ridge National Laboratory, Oak Ridge Tennessee, USA

(Dated: 27 December 2017)

A collection of routines for calculation of the total cross section that determines the attenuation of neutrons by crystalline solids is presented. Total cross section is calculated semi-empirically as a function of crystal structure, neutron energy, temperature, and crystal orientation. The semi-empirical formula includes the contribution of parasitic Bragg scattering to the total cross section using both the crystal's mosaic spread value and its orientation with respect to the neutron beam direction as parameters. These routines allow users to enter a distribution of crystal orientations for calculation of total cross sections of user defined powder or pseudo powder distributions, which enables simulation of non-uniformities such as texture and strain. The spectra for neutron transmission simulations in the neutron thermal energy range (2 meV to 100 meV) are presented for single crystal and polycrystal samples and compared to measurements.

This manuscript has been authored by UT-Battelle, LLC under Contract No. DE-AC05-00OR22725 with the U.S. Department of Energy. The United States Government retains and the publisher, by accepting the article for publication, acknowledges that the United States Government retains a non-exclusive, paid-up, irrevocable, world-wide license to publish or reproduce the published form of this manuscript, or allow others to do so, for United States Government purposes. The Department of Energy will provide public access to these results of federally sponsored research in accordance with the DOE Public Access Plan (<http://energy.gov/downloads/doe-public-access-plan>).

PACS numbers: Valid PACS appear here

Keywords: neutron diffraction, neutron transmission, single crystal neutron transmission, neutron Bragg edges, neutron transmission simulation

I. INTRODUCTION

Soon after the first demonstration experiment of neutron diffraction¹, the problem of neutron transmission through crystalline materials was first theoretically approached by Halpern, Hamermesh and Johnson². However, the first experimental results were published only after the world war by Fermi, Sturm and Sachs³. They reported the energy dependence of neutron transmission through polycrystalline Be and BeO, characterized by "violent fluctuations for small changes in the energy" (Bragg edges). This behavior was successfully reproduced based on neutron coherent elastic scattering calculations pioneered by the previous authors². As the main purpose of these initial works was to determine material properties accounting for the interaction with neutrons (impacting the reactor physics), some sources of errors have also been envisioned from the beginning: extinction and preferential orientation (crystallographic texture). Later, the neutron transmission through crystals and polycrystals became a concern of neutron optics, in high demand for the emerging neutron scattering field, in need of neutron monochromators and filters⁴. It is strange that the idea of using neutron transmission as a tool for materials studies was advanced only in the late 1980s by Bowman & Priesmeyer. With the advent of pulsed neutron sources, after pioneering real-time experiments at LANSCE⁵, the neutron time-of-flight transmission method received a larger audience and benefited from a sound theoretical background and software development⁶. Two seminal papers^{7,8}, published at the beginning of the century, defined the field, followed by

many others.

Simultaneously, the improvement in the technology of neutron detectors ensured a tremendous increase of spatial resolution and neutron imaging became a mainstream technique for neutron applications⁹. In this environment, the idea of using an energy dispersive method in neutron imaging was enthusiastically welcomed. A few demonstration studies, performed with a low spatial resolution, assessed the possibility of performing 3D imaging (tomography) of phase content¹⁰ or strain¹¹ by analyzing the energy dependence of transmission images. Two efficient experimental approaches were developed soon after: (1) at steady-state research reactors, using double crystal monochromators¹² (13.5 μm spatial resolution and 3% wavelength resolution); and (2) at pulsed neutron sources, using the time-of-flight method¹³ (55 μm spatial resolution and 0.4% wavelength resolution).

The complexity of obtaining tomographic information for strain, particle size and orientation are well documented within the literature. Woracek¹⁴ has shown the feasibility of obtaining crystalline phases via energy-selective neutron computed tomography (CT). For strain tomography and texture analysis, the directional nature of these parameters results in a voxel within the sample having a cross section that varies with viewing direction, and as a result prevents the use of traditional CT reconstruction techniques that assume constant cross section for all orientations in the neutron beam. For further understanding of the transmission models and to create general CT capabilities, both measurements and simulations are needed.

^{a)}Electronic mail: Dessieuxll@ornl.gov

^{b)}Electronic mail: Stoicaad@ornl.gov

^{c)}Electronic mail: Binghampr@ornl.gov

The studies on attenuation of thermal and cold neutrons beams in large single crystals were inspired

by the necessity of predicting the performance of neutron filters (see Adib¹⁵ and references therein). In these studies, the crystals are considered ideally imperfect (mosaic) and the reflecting power of each crystallographic plane is evaluated under a secondary extinction assumption¹⁶ (Darwin equation). In fact, the reflectivity expressions used for crystal plates were first deduced by Bacon & Lowde¹⁷ (in Bragg geometry) and Dietrich & Als-Nielsen¹⁸ (in Laue geometry). The effect of diffraction on transmission was evaluated by subtracting the reflectivity from unity, and the other contributions to attenuation (absorption, inelastic scattering) were considered independently. However, the exact solutions of the Darwin equation for transmissivity through a single crystal plate were later reported by Sears¹⁹, and it was shown that, in the Bragg geometry, the non-diffractive attenuation cannot be decoupled from the diffraction attenuation (anomalous absorption).

The neutron cross section modeling under a powder assumption²⁰ proved to be suitable for treating the transmission data in a similar way as the Rietveld approach⁶, which is extensively used in powder diffraction. The Rietveld-type codes include extinction corrections²¹ inspired by an earlier work of Sabine²². In this approach, only the primary extinction plays a role in polycrystalline materials and secondary extinction has no meaning, as all orientations of mosaic blocks are present with equal probability. Such an assertion is valid only if the number of mosaic blocks (coherent domains) per each grain is quite small; it may be true for brittle materials but not for metals, for which each grain includes significantly smaller blocks (usually well below 1 μm). In general, the primary extinction length exceeds a few μm even for the most powerful diffraction lines; this is why the primary extinction corrections are rarely used in neutron powder diffraction. The primary extinction corrections were automatically extended to the Rietveld-type transmission codes²³ and are used to estimate grain size in ductile materials. On the other hand, the secondary extinction is clearly necessary to predict the neutron transmission through single crystals but is not considered for polycrystals. It is true that the secondary extinction length is usually in the sub-millimeter or millimeter range for normal diffractometer arrangements, but it can reach μm values close to back reflection. Thus, as the secondary extinction length can become comparable to or less than grain size (tens of μm), there are instances when it should be considered in transmission, even for polycrystalline samples.

In this paper, we present a simulation algorithm for neutron transmission through crystalline samples. Our model calculates the neutron transmission for each grain in a given grain distribution within a voxel, and the transmission values are combined to obtain the total transmission within the voxel. We illustrate the capability of our simulation by comparing the neutron transmission of a single crystal Cu with recently published experimental data^{7,24}. The ability to generate polycrystalline transmission patterns is also demonstrated and compared to experimental data measured at the VULCAN^{25,26} in-

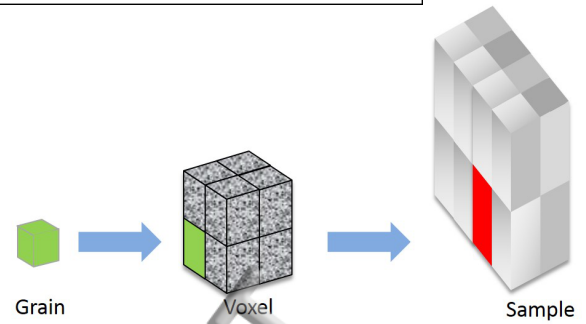


FIG. 1. Each grain cross section is calculated, a distribution of grains is aggregated to form voxel cross-section, with voxel cross sections a sample can be simulated.

strument located at the Spallation Neutron Source(SNS), Oak Ridge Tennessee; we analyze the limitations imposed by the grain-size distribution on quality of transmission data recorded for engineering applications.

II. SIMULATION METHODOLOGY

Traditionally, neutron Bragg edge transmission²⁷ through polycrystalline samples is calculated as a function of the path length through the sample and the attenuation coefficient of the material. The attenuation coefficient is directly proportional to the total neutron cross section, which is described as the summation of the coherent cross section, the thermal diffuse cross section and the absorption cross section. For neutron Bragg edge calculation, the coherent cross section is of importance and is a function of wavelength, crystal parameters such as lattice spacing and structure factor. This work assumes the sample is discretized into voxels of uniform size as shown in Figure 1. Our model calculates the neutron transmission for a given grain distribution within a voxel by calculating transmission for each individual grain in the distribution and combining these for a total voxel transmission value. The neutron transmission through the voxel is written as contribution of all the grains

$$T_t(\lambda) = \text{Combined} \left\{ T_i \left(g, \tau, W(\theta - \theta_B), \xi, \omega, \lambda \right) \right\} \quad (1)$$

where T_i is the neutron transmission calculation of a grain as function of the grain orientation g , the grain size τ , the mosaic distribution within the grain W , θ is the current angle between the incident beam and Bragg planes, θ_B is the nominal Bragg angle, the wavelength λ , the crystal parameters (ξ), and material parameters (ω). With this approach the user can define distinct grain distributions within a polycrystalline material to model complex materials with texture, strain and mixtures. Figure 2 shows a high level flow chart for the general approach of the simulation algorithm. The dashed line area in the flow chart contains the different input blocks that are required for the simulation of the neutron transmission spectra; the crystal and sample orientation block describes the necessary transformation to orient the crystal within the sample and the sample to

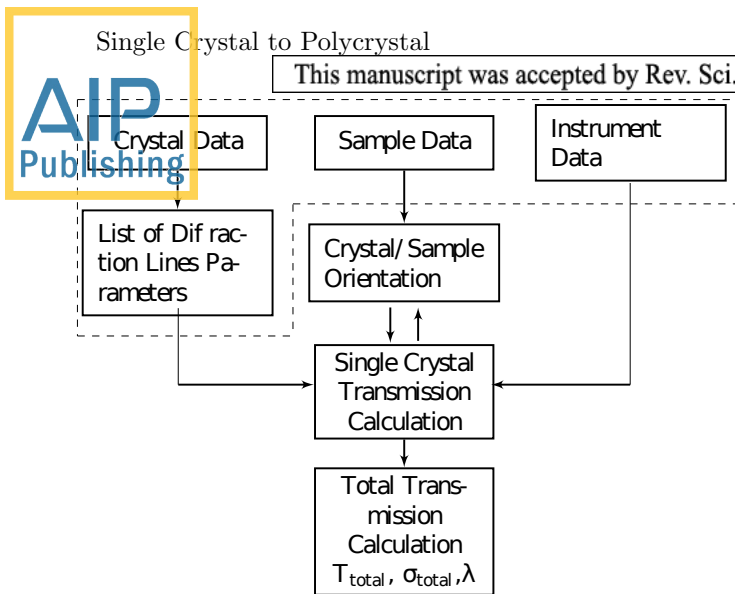


FIG. 2. Schematic of *sinpol* architectural organization.

the laboratory system; the single crystal neutron transmission calculation block contains the necessary physics calculations for the neutron transmission of a single grain; finally the total transmission calculation block illustrates the manner in which the neutron transmission values for each grain in a population are combined to calculate the neutron transmission spectra thorough a voxel. In this section we have described each of these blocks in more detail.

A. Input Parameters

As shown in the dashed area of Figure 2, input parameters consist of crystal parameters, sample parameters and instrument parameters. Crystal data parameters that contain structural, neutronic, and mesoscale modelling information are entered to calculate the list of diffraction lines parameters that are essential for single crystal neutron transmission calculation. Crystal structural information is obtained by using a space group symbol, which can be entered as space group number, or alternatively as Schoenflies or HermannMauguin symbol. The crystal symmetry information (e.g. cubic, hexagonal or orthorhombic) is obtained from the space group information using the Computational Crystallography Toolbox²⁸. The free-atom positions of the unit cell are obtained from the ASE²⁹ library. Once the crystal structure is determined, the lattice spacings for each reciprocal lattice direction are calculated. Neutron cross section information such as the linear absorption coefficient, coherent length (b_{coh}), and bound cross section are obtained from Sears³⁰. The mosaicity is implemented by calculating an angular spread in the current Bragg angle, θ , relative to the nominal Bragg angle, θ_B , using a normalized two-dimensional Gaussian function. In this paper, the width of the mosaic distribution is quantified by its full width at half maximum (FWHM) value.

Secondly, the sample data parameters for the current simulation tool includes the crystal orientation

distribution. The crystal orientation distribution defines whether a single crystal or a polycrystalline material is simulated. Each single crystal orientation is entered as three Euler angles that define the crystal orientation within the sample's system, using the Bunge³¹ nomenclature. A random distribution of single crystal orientations can be used to define a polycrystalline powder, or an orientation distribution function based on texture components can be used to define a textured polycrystalline aggregate. In this work defined here, the Halton sequence³²(see Appendix A) is used to generate a uniform orientation distribution.

Finally, the instrument data input includes a wavelength distribution defining the neutron source (the incident neutron wavelength and the incremental wavelength steps necessary for the neutron transmission calculation), the wavelength resolution of the instrument, and an angle that defines the sample orientation within the instrument coordinate system.

B. Orientation of Crystals and Sample

In order to simulate neutron transmissions spectra, it is necessary to define the orientation of the crystals within the voxel and the orientation of the voxel in the neutron beam. These three dimensional rotations are performed in the crystal/sample orientation block of the flow chart. Two rotations are necessary to calculate the direction cosine of the incident beam γ_o and the diffracted beam γ_H , which are essential for transmission calculations. The following subsections describe rotation of grains in a voxel, rotation of the sample in the instrument, and calculations of angular directions for each lattice plane in a grain.

1. Crystals Within Voxel Orientation

Our simulation code uses standard orientation matrices. The orientation matrix is constructed from a series of ordered rotations parameterized with Euler angles, with each Euler angle describing a rotation about one axis. Several conventions can be used to describe the Euler rotations; here the Bunge³¹ convention is used to construct the orientation matrix. In this convention, both sample and crystal coordinate system are expressed in cartesian coordinates. At first the crystal coordinate system is parallel to the sample coordinate system, and the orientation matrix is constructed via matrix multiplication such that a crystal orientation g can be written as a rotation about the Z axis by ϕ_2 , followed by a rotation Φ about the new X axis and a final rotation about the new Z axis by ϕ_1 .

$$a = g_{\phi_1 Z} g_{\Phi X} g_{\phi_2 Z} = \begin{pmatrix} a_{11} & a_{12} & a_{13} \\ a_{21} & a_{22} & a_{23} \\ a_{31} & a_{32} & a_{33} \end{pmatrix} \quad (2)$$

The rotation matrix³³, a , is the product of the three rotations and is the orientation matrix that links the crystal reference vector basis to the sample vector basis as shown by Bunge³¹. Thus the rotation of a lattice vector with reciprocal lattice coordinates h, k, l into the sample frame of reference Y_j^S can be performed and the lattice vector \vec{h} can be written as

$$\vec{h} = \sum_j \tilde{h}_j^S Y_j^S; \quad \tilde{h}_j^S = \sum_i \tilde{h}_i a_{ij} \quad (3)$$

where \tilde{h}_i is the normalized direction cosines corresponding to the hkl Miller indices.

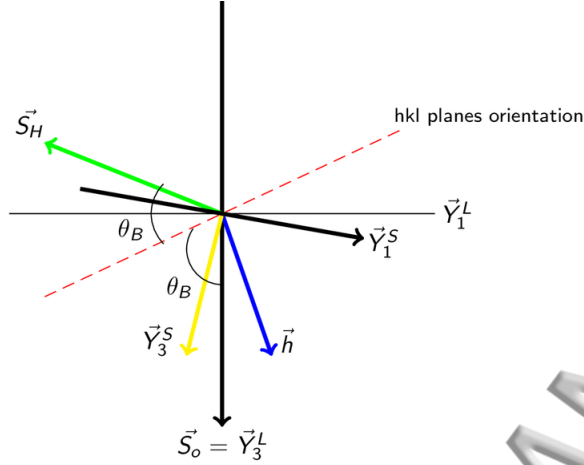


FIG. 3. Scattering path in a plane-slab crystal, showing the relationship between the diffraction beam S_H and the incident beam S_o , and the relationship between the incident beam S_o and the sample's normal Y_3^S .

2. Relationship Between The Laboratory Coordinate System and The Sample Coordinate System

While a sample can be positioned in any orientation within the instrument frame, the initial code assumes the simplest case of a rotation about the vertical axis ($R_{\rho Y}$), which mimics the common practice of rotation around a single axis for CT scanning. Thus the reciprocal lattice vector \vec{h} in the laboratory frame is written as

$$\vec{h} = \sum_j \tilde{h}_j^L Y_j^L, \quad (4)$$

where

$$\tilde{h}^L = \{\tilde{h}_1^S, \tilde{h}_2^S, \tilde{h}_3^S\} \begin{pmatrix} \cos \rho & 0 & -\sin \rho \\ 0 & 1 & 0 \\ \sin \rho & 0 & \cos \rho \end{pmatrix} \quad (5)$$

and ρ is the rotation angle. The reference orientation of the sample in the laboratory (instrument) frame considers the z axis of the sample along the neutron beam and the y axis perpendicular to the horizontal plane.

3. Calculation of Direction Cosines

The angle between the normal to the crystallographic surface and the neutron beam is the diffraction angle θ_B , therefore the sine of θ_B is given as

$$\sin \theta_B = -\tilde{h}_1^S \sin \rho + \tilde{h}_3^S \cos \rho. \quad (6)$$

Using equation (6) Bragg's law can be written as

$$\lambda_B = 2d_{hkl} \sin \theta_B, \quad (7)$$

where d_{hkl} is the spacing between hkl planes.

The diffraction intensity has dependency on the direction cosines of the incident beam to the surface of the crystal γ_o and the diffracted beam γ_H . Figure 3 illustrates the geometry of the incident beam impinging on a crystal hkl plane; S_o and S_H are respectively the incident beam and diffracted beam. Here the direction cosine of the incident beam is the dot product of the sample's normal vector \vec{n}_s and the incident neutron beam S_o ; simply put γ_o is written as

$$\gamma_o = \vec{n}_s \cdot S_o = Y_3^S \cdot Y_3^L = \cos \rho. \quad (8)$$

The direction cosine of the diffracted beam is the dot product between the sample's normal \vec{n}_s and S_H the diffracted beam as

$$\gamma_H = \vec{n}_s \cdot S_H = Y_3^S \cdot S_H = \cos \rho - 2 \sin \theta_B \tilde{h}_3^S, \quad (9)$$

where γ_H determines the choice between Bragg geometry and Laue geometry, a value greater than zero indicates Laue geometry. In the reference orientation of the sample, Y_3^S is parallel to S_o , γ_o is equal to 1, and γ_H is $\cos 2\theta_B$.

C. Single Crystal Neutron Transmission Calculation

Once grains have been oriented with the neutron beam, calculation of cross section for each grain is performed by first calculating the transmission for each reciprocal lattice point near the Ewald sphere and then combining lattice transmissions to get a total grain transmission. When multiple reciprocal lattices are lying near the Ewald sphere, we derived an approximation for the total transmission.

The diffraction profiles of mosaic crystals display peaks that are broader and lower in peak intensity when compared to the diffraction profile of perfect crystals. Zachariasen³⁴ and Bacon³⁵ have calculated the reflection powers for imperfect crystals. Both assumed a symmetrical approach where the incident and the diffracted beams make the same angle at the surface of the crystal slab, in which the reflecting planes are either parallel or perpendicular to the surface of the crystal. In the case where the reflecting planes are neither parallel nor perpendicular to the surface, the reflection power has been calculated by Dietrich and Nielsen¹⁸. A more general solution

of these equations has been formulated by Sears¹⁹. Sears equations for reflected R_{hkl} and transmitted T_{hkl} beam intensities in the Bragg geometry are given by

$$R_{hkl}(\lambda) = \frac{b}{\frac{(a+b)}{\Gamma} + A \coth(A)} \quad (10)$$

$$T_{hkl}(\lambda) = \frac{\sqrt{\frac{(a+b)^2}{\Gamma^2} e^{-\frac{a+b}{G}}}}{\frac{(a+b)}{\Gamma} \sinh(A) + \sqrt{\frac{(a+b)^2}{\Gamma^2} - \frac{b^2}{\gamma_o \gamma_H} \cosh(A)}}, \quad (11)$$

and in the Laue case by

$$R_{hkl}(\lambda) = \frac{e^{-\frac{(a+b)}{\Gamma}} b \sinh(S)}{S} \quad (12)$$

$$T_{hkl}(\lambda) = e^{-\frac{(a+b)}{\Gamma}} \left[\cosh(S) - \frac{a+b}{G} \sinh(S) \right]. \quad (13)$$

The following auxiliary quantities are used in the Sears¹⁹ solutions:

$$a = \frac{\mu\tau}{\gamma_o} \quad (14)$$

$$b = \frac{\sigma\tau}{\gamma_o} \quad (15)$$

$$\frac{1}{G} = \frac{1}{2} \left(\frac{1}{\gamma_o} - \frac{1}{\gamma_H} \right) \quad (16)$$

$$\frac{1}{\Gamma} = \frac{1}{2} \left(\frac{1}{\gamma_o} + \frac{1}{\gamma_H} \right) \quad (17)$$

$$A = \sqrt{\frac{(a+b)^2}{\Gamma^2} - \frac{b^2}{\gamma_o \gamma_H}} \quad (18)$$

$$S = \sqrt{\frac{(a+b)^2}{G^2} + \frac{b^2}{\gamma_o \gamma_H}}, \quad (19)$$

where the crystal's thickness τ , the attenuation coefficient μ , and the Bragg reflection coefficient σ are the physical quantities that govern diffraction by mosaic crystals. $\sigma = QW[\theta - \theta_B]$ is the cross section per unit volume for Bragg reflection, where $Q = \lambda^3 F_{hkl}^2 N_c^2 / \sin 2\theta_B$, with λ the neutron wavelength, F_{hkl} the structure factor and N_c the number of unit cells per unit volume. $W[\theta - \theta_B]$ is the mosaic distribution usually assumed to be Gaussian, with θ being the angle formed by the incident beam and the Bragg planes and θ_B is the nominal Bragg angle.

When there are no Bragg reflections present, R is zero in both Bragg and Laue geometry, and the transmission T is the recognizable Lambert law:

$$T_{hkl}(\lambda) = e^{-\mu(\lambda)\tau}. \quad (20)$$

In this case, the probability of a neutron being removed from the incident beam is proportional to the attenuation coefficient μ , which can be written as the sum of nuclear absorption and thermal diffuse scattering

$$\mu(\lambda) = \frac{n}{v_0} (\sigma_{abs}(\lambda) + \sigma_{tds}(\lambda)), \quad (21)$$

where n is the number of atoms in the unit cell, v_0 is the volume of the unit cell, and σ_{abs} is the absorption cross section, which is written as

$$\sigma_{abs}(\lambda) = \frac{C_1}{\sqrt{E}}, \quad (22)$$

where C_1 is a constant, and E is the neutron energy.

The thermal diffuse cross-section (σ_{tds}) can be calculated as the sum of single phonon and multiple phonon cross-sections: $\sigma_{tds} = \sigma_{singleph} + \sigma_{multiph}$. At lower energy, the thermal diffuse cross section is dominated by the single phonon $\sigma_{singleph}$. At intermediate energies, interference from multiple sites must be considered. In this work, the formalism of Freund³⁶ is used to calculate the thermal diffuse cross section.

For single crystals, Sears treated the case in which there is solely one reciprocal lattice plane on the Ewald sphere. As shown by Renniger³⁷ and Moon & Shull³⁸, there are instances in which the incident beam will interact with multiple lattice planes. Following Rossmannith's³⁹ approach to Renniger's³⁷ kinematic approximation in the three-beam case, the total reflection can be approximated as

$$P^{three-beam}(\lambda) = P_o(k_{hkl} + k_{hkl'} - 2k_{hkl}k_{hkl'}), \quad (23)$$

where P_o is the power of the incident beam and $k_{hkl, hkl'}$ are partial reflectivities. In the case where absorption is not present, equation (23) can be written in terms of transmission as

$$T_i(\lambda) = (T_{hkl}T_{hkl'} + (1 - T_{hkl})(1 - T_{hkl'})). \quad (24)$$

T_{hkl} and $T_{hkl'}$ are the partial transmission coefficients calculated for the two-beam case. The approximation of equation 23 is valid only when k_{hkl} and $k_{hkl'}$ are small, rendering equation 24 valid only when transmission values T_{hkl} and $T_{hkl'}$ are large (.5 or greater). In the region where the transmission values T_{hkl} and $T_{hkl'}$ are small (less than .5), equation (24) gives an unphysical result, and a correction to the Renniger approximation has to be implemented as

$$P^{threeBeam}(\lambda) = P_o(k_{hkl} + k_{hkl'} - xk_{hkl}k_{hkl'}), \quad (25)$$

which modifies the transmission formula to

$$T_i(\lambda) = T_{hkl}T_{hkl'} + (x - 1)(1 - T_{hkl})(1 - T_{hkl'}). \quad (26)$$

The solution for the coefficient x must go to 1 for small transmission values, and at large transmission values x must approach the value of 2. We consider a simple but not distinct solution for x given as

$$x = \frac{T_{hkl} + T_{hkl'}}{T_{hkl} + T_{hkl'} - T_{hkl}T_{hkl'}}. \quad (27)$$

Substituting x into equation 26 and generalizing for the j^{th} lattice plane, which lies near the Ewald sphere, the transmission for a grain can be approximated using

$$T_i(\lambda) = \frac{1}{\sum_j (\frac{1}{T_j} - 1) + 1}. \quad (28)$$

D. Total Neutron Transmission Calculation

The final block in the Figure 2 flow chart combines the transmission from many grains in a single voxel. A polycrystal solid is composed of many crystallites of varying size and orientations. Equation 1 introduced the 'Combined' function of transmission from each grain. In this section, we demonstrate the approach to combine transmission for grains in a serial arrangement as well as for grains in a parallel arrangement within a voxel. In this work a polycrystal is defined by means of segmenting an infinite plate into columns consisting of N orientations with grain size defined as the ratio of number of orientation in a column to the thickness of the plate as illustrated in Figure 4. The transmission of each individual column with N orientations with the neutron beam is written as

$$T_c(\lambda) = \prod_{i=1}^N T_i(\lambda). \quad (29)$$

The transmission for a plate segmented into a number of columns A is written as the average over all the columns.

$$T_{total}(\lambda) = \frac{\sum_{j=1}^A \prod_{i=1}^N T_{i,j}(\lambda)}{A} \quad (30)$$

By implementing equation 30, the simulator allows users to study partial volume effects.

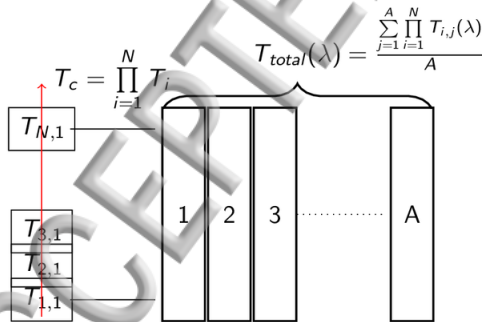


FIG. 4. Segmented plate with A columns and with columns containing N distinct grain orientations. Each grain transmission is calculated, a distribution of grains is aggregated to form voxel transmission; with voxel transmission, a sample's transmission can be calculated

III. MODEL RESULTS AND DISCUSSION

For verification of the simulator, simulations of single crystal and polycrystalline materials are presented in the

following sub sections.

A. Single Crystal Cu Simulation

The neutron transmission spectra for a large imperfect single crystal of copper plate that is 10 mm thick and has mosaic spread of 0.2 degrees has been simulated. The main physical parameters required in the calculation are crystal lattice parameters, the Debye temperature Θ_D , the neutron coherent scattering length b , the neutron absorption cross section σ_{abs} , and the total bound scattering cross section σ_b . The values for the required physical parameters are shown in Table I. Similar to the measurements presented by Santisteban⁷, the simulated crystal is cut along the (110) plane and positioned such that the cosine of the (hkl) normal to the beam direction is given as

$$\sin \theta_B = \frac{\tilde{h} + \tilde{k}}{\sqrt{2}}, \quad (31)$$

where \tilde{h} and \tilde{k} are the normalized h, k values given below for the cubic crystal structure of copper

$$\tilde{h} = \frac{h}{\sqrt{h^2 + k^2 + l^2}}; \tilde{k} = \frac{k}{\sqrt{h^2 + k^2 + l^2}}. \quad (32)$$

Figure 5 presents wavelength-dependent transmission simulation results depicting the movement of peak locations and intensity as a function of crystal rotation. The crystal is rotated 180 degrees around the transverse (vertical) direction. These simulation results show the behavior of diffraction hkl peaks during rotation. When hkl peaks are closest to the Bragg edge condition, they show the highest intensity, and the broadening induced by mosaic is less pronounced. When hkl peaks rotate away from the Bragg edge condition ($\sin \theta_B = 1$), lower peak intensity and peak broadening due to mosaic are observed. At the Bragg edge location, the diffraction peak is sharp and can be resolved only by considering the resolution of the instrument. The *sinpol* simulation uses a Gaussian for the instrument function which is convolved with the simulated intensity. The gray-shaded area in Figure 5 corresponds to the range of rotation angles presented by Santisteban⁷. Here the rotation ranges from 88 to 91 degrees. The simulation corresponds well with the initial measurement by Santisteban⁷, and the simulated angles of interest are displayed in figure 6. As outlined in Santisteban⁷, the reduction of the incident beam intensity is governed by nuclear absorption and thermal diffuse scattering. The temperature-dependent thermal-diffuse scattering dominates at the shorter wavelength, while the temperature independent neutron absorption is linear and dominates at longer wavelengths. The Bragg reflections are seen as sharp peaks at precise wavelengths that can be calculated by using the alternative Bragg equation

$$\lambda_{hkl} = 2d_{hkl} \frac{\tilde{h} + \tilde{k}}{\sqrt{2}}. \quad (33)$$

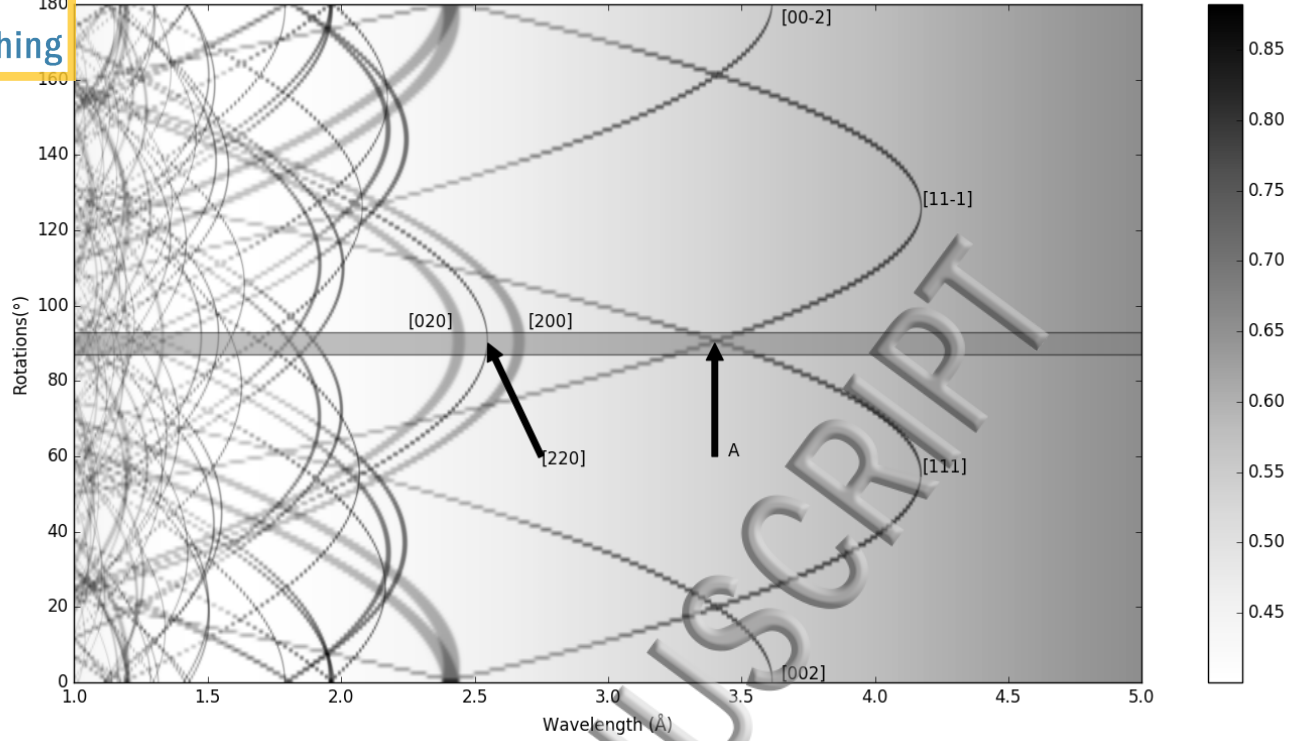


FIG. 5. Movement of peak locations and intensity as a function of crystal rotation for a single crystal.

TABLE I. Physical parameters

Element	Crystal structure	atomic mass	Lattice constant(Å)	Θ_D (k)	b(fm)	σ_{abs} (barns)	σ_b (barns)
Cu	fcc	63.55	3.61496	344	7.718	3.78	8.035
Fe	bcc	55.45	2.8665	477	9.45	2.56	11.62
Ni	fcc	58.69	3.52	345	10.3	4.49	18.5

The bottom of Figure 6 shows three discrete simulated rotations matching Santisteban's measurements. As the crystal is rotated by one-degree increments, the [200], [220] and [020] peaks remain stationary, as they are at an orientation where the angle between the reciprocal lattice vector and the neutron beam direction varies slowly with the sample's rotation. Further examination of Figure 5 shows that as the crystal is rotated, eventually the [200], [220], and [020] peaks will move toward shorter wavelengths, as the crystal's ND alignment with the beam is not perfect. [111] and [11-1] peaks show a noticeable movement in wavelengths moving toward shorter wavelengths and larger wavelengths respectively. The area labeled A in Figure 5 indicates a multi beam scenario in which multiple Bragg reflections occur at the same wavelength. The transmission intensity is calculated to include contributions from multiple planes, using equation 28.

Table II shows the comparison of the peak locations in wavelengths measured from Santisteban⁷ and the peak location from the singpol simulation. The difference between the *sinpol*-simulated positions and the experimental positions varies from a maximum of 0.43 percent difference at peak [200] to a minimum difference of 0.01

TABLE II. Typical parameters of the peaks observed in (1-T), simulated along the [110] direction of the reference copper sample and compared to measurement by Santisteban⁷

hkl	λ_{hkl}^7	λ_{hkl}^{sp}	Θ_B^7	Θ_B^{sp}
[111]	3.4366	3.4462	34.456	34.350
[11 $\bar{1}$]	3.3676	3.3621	36.184	36.345
[020]	2.6760	2.6691	42.219	42.409
[220]	2.5521	2.5531	2.74	2.786
[200]	2.4268	2.4372	47.807	47.608
[131]	1.9101	1.9105	28.76	28.789
[13 $\bar{1}$]	1.8917	1.8875	29.752	30.017
[311]	1.8197	1.8261	33.371	33.100
[31 $\bar{1}$]	1.8013	1.8032	34.241	34.189
[222]	1.7179	1.7231	34.567	34.350
[22 $\bar{2}$]	1.6840	1.6811	36.173	36.345
[331]	1.6170	1.6191	12.757	12.530
[33 $\bar{1}$]	1.6062	1.6059	14.347	14.494
[240]	1.5558	1.5551	15.679	15.865
[420]	1.5063	1.5086	21.232	21.058

percent at peak [131], with an average peak difference of 0.062 percent over all peaks. The precision for the simulated peak positions can potentially be improved by adjusting the three Bunge angles to more precisely

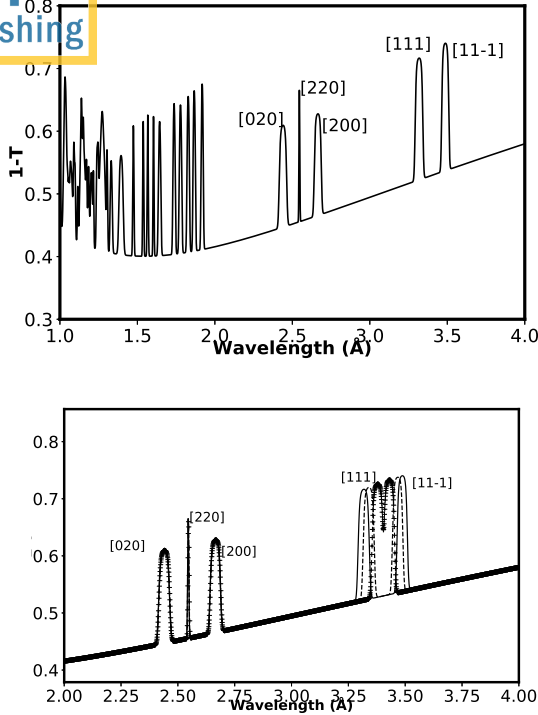


FIG. 6. (top), Neutron transmission spectra of single copper crystal. (bottom), Shifts in peak position as a result of rotation of sample, solid line the incident beam is aligned with [110] direction, dash line sample is rotated by 1 and 2 degree in the transverse direction.

match the crystal orientation in the measurement.

In a later paper, Malamud and Santisteban²⁴ introduced an extinction factor, which is dependent on the experimental geometry, the divergence of the beam, as well as the mosaicity of the sample. The extinction factor, y_{hkl} , is the ratio of the measured intensity to the predicted kinematical intensity, therefore it represents the reduction in measured intensity due to the effect of extinction. Table III shows the comparison of the peak locations in wavelengths measured from Malamud²⁴ and the peak location from the *sinpol* simulation. The difference between the *sinpol*-simulated positions and the experimental positions varies from a maximum of 2.5 percent difference at peak [204] to a minimum difference of 0.1 percent at peak [111], with an average peak difference of 0.9 percent over all peaks. Column four is the reproduction of the extinction factor y_{hkl} , determined experimentally by Malamud²⁴. The extinction factors calculated by *sinpol* differ slightly from the experimental values reported in Table III in reference²⁴; *sinpol* uses a gaussian instrumental function to convolve the simulated intensity while Malamud and Santisteban²⁴ used a truncated exponential convoluted to a gaussian to measure intensity. The difference in the two fit functions may lead to intensity of simulated peaks in *sinpol* being larger and affecting the extinction ratio. The last two columns present the measured and simulated peak fwhm ω , which are in a good agreement.

TABLE III. Refined and derived peak parameters for the copper sample and compared to measurement by Malamud²⁴

hkl	λ_{hkl}^{24} (Å)	λ_{hkl}^{sinpol} (Å)	y_{hkl}^{24}	y_{hkl}^{sinpol}	ω^{24}	ω^{sinpol}
[111]	3.442	3.4439	0.004	0.0033	0.02	0.018
[1-11]	3.358	3.3549	0.004	0.0033	0.021	0.018
[200]	2.72	2.7103	0.007	0.0056	0.019	0.019
[202]	2.55	2.5402	0.006	0.0045	0.008	0.008
[002]	2.38	2.3868	0.010	0.0074	0.021	0.022
[311]	1.928	1.9178	0.020	0.0235	0.01	0.01
[3-11]	1.905	1.8902	0.020	0.0242	0.01	0.012
[113]	1.804	1.7917	0.024	0.0257	0.011	0.011
[1-13]	1.781	1.7707	0.024	0.0306	0.011	0.011
[222]	1.721	1.7107	0.028	0.0326	0.011	0.012
[2-22]	1.679	1.6663	0.025	0.0354	0.011	0.011
[313]	1.617	1.5821	0.023	0.0356	0.006	0.0066
[3-13]	1.604	1.5682	0.023	0.0382	0.006	0.0066
[402]	1.564	1.5315	0.022	0.0425	0.006	0.0066
[204]	1.496	1.4542	0.031	0.0526	0.007	0.007
[220]	1.391	1.3888	0.039	0.0356	0.016	0.015
[400]	1.36	1.3445	0.039	0.0578	0.01	0.01

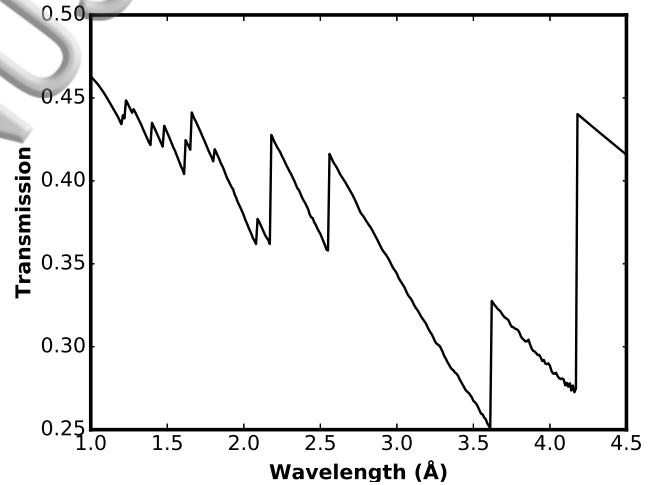


FIG. 7. Simulated copper neutron transmission with 10 million distinct crystallites orientations.

B. Polycrystalline Simulation

The thermal neutron transmission spectra of imperfect single crystals display low-intensity valleys, which are direction-dependent based on the oriented regions of the mosaic blocks; the thermal neutron transmission spectra of polycrystalline materials shows sudden well-defined increase in intensity as a function of neutron wavelength. These steep increases in neutron transmission intensity are normally referred to as Bragg edges, and these Bragg edges materialize at wavelength locations that exceed the Bragg condition for coherent scattering by certain lattice planes. The position, height, and slope of the so called Bragg edges are dependent on the number of crystallites oriented along the line of the neutron beam through the material being investigated. In this work, the simulation of a polycrystal copper sample is represented by segmenting a 1-cm-thick plate into

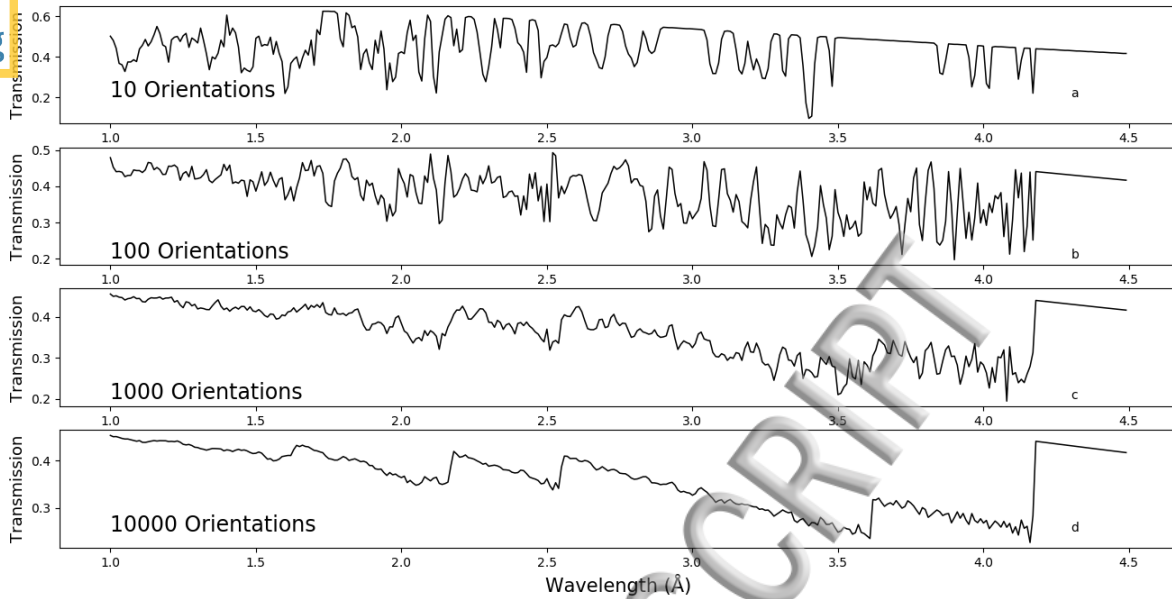


FIG. 8. Copper neutron transmission for 10 distinct crystallites orientations, 100 distinct crystallites orientations, 1000 distinct crystallites orientations and 10000 distinct crystallites orientations.

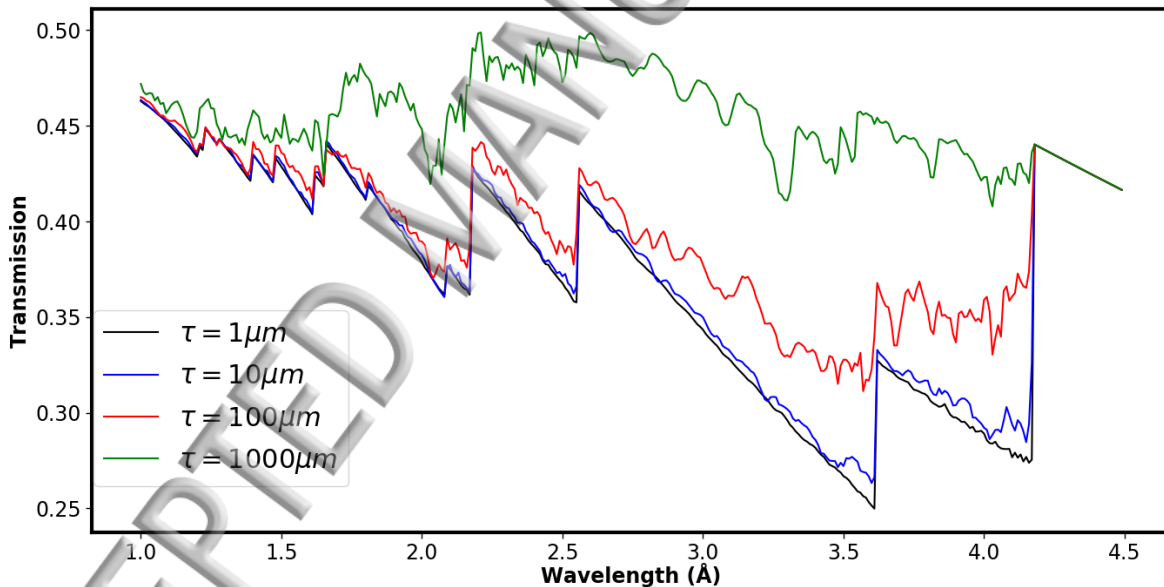


FIG. 9. Neutron transmission simulations of copper polycrystals, with grain sizes of $\tau = 1000\mu\text{m}$, $\tau = 100\mu\text{m}$, $\tau = 10\mu\text{m}$, and $\tau = 1\mu\text{m}$.

1000 columns. Each column contains 10,000 distinct orientations with a uniform angular distribution. This setup represents the interaction of the neutron beam with a voxel of 10 millions crystallites with distinct orientations, and the simulation result is shown in Figure 7. The *simpol* simulation shown in Figure 7 resembles the neutron transmission spectra for copper measured in Kockelmann⁴⁰, the shape and Bragg edge locations are comparable. The high-frequency noise observed in the experimental data shown by Kockelmann⁴⁰ is due to neutron statistical noise, which is not included in the simulations.

Simulations were performed to help determine impact of the number of crystal orientations on simulation results and to illustrate the effect of secondary extinction on polycrystalline neutron transmission. Figure 8 presents the calculated neutron transmission spectra for one column of a 1-cm-thick copper plate, with varying numbers of crystal orientations including 10, 100, 1000 and 10,000 orientations. The neutron transmission spectra for 10 and 100 distinct orientations are comparable to single crystal spectra, with well-defined peaks dependent on the crystallite orientations. The neutron

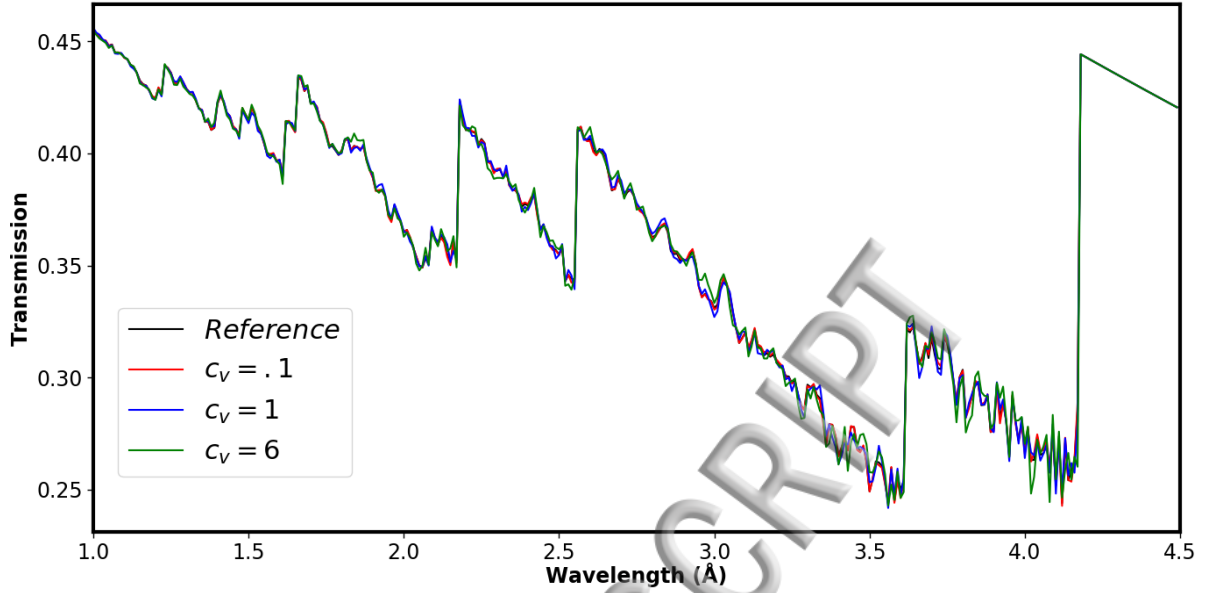


FIG. 10. Neutron simulation through a 1-cm copper plate using a log-normal distribution to represent the grain size, with varying b_{LN} ; the mean size τ_v was kept to $1 \mu\text{m}$.

spectra for 1000 distinct orientations displays a coarse spectra for a copper powder, with Bragg edges starting to stand out. The *singpol* calculations for 10,000 distinct orientations is consistent with the measured neutron transmission spectra for copper found in Kockelmann⁴⁰ and those calculated in Figure 7. The high-frequency noise observed in the simulation is a result of the randomness or lack thereof in the distribution. The lack of diffraction above 4.2 angstroms results in a smooth line.

Figure 9 presents the neutron transmission simulation spectra for a 1-cm-thick copper plate segmented 1,000 times, with each segment consisting of a single column, with varying numbers of distinct crystal orientations including 10,100,1000 and 10,000. The neutron transmission of the four different numbers of orientations of grains per column represents the neutron simulation of polycrystals, with grain sizes of $1000\mu\text{m}$, $100\mu\text{m}$, $10\mu\text{m}$, and $1\mu\text{m}$ respectively. Simulations were performed to help determine the impact of grain sizes on neutron transmission simulation results and to illustrate the effect of extinction on polycrystalline neutron transmission. The difference in simulated neutron transmission intensity shown in Figure 9 illustrates the extinction effect on neutron transmission measurements. As the grain size decreases, the transmission intensity decreases. The extinction effect simulated here is less drastic than those reported by Sato²³ and are concentrated about the neutron Bragg Edges.

Based on the simulation data presented in Figure 8, it can be concluded that the number of grains probed in neutron transmission measurements may be of concern for the Bragg edge imaging method. If we consider 10^4 grains as a threshold value for visualizing the four first Bragg edges in a fcc material, the extension of the image

pixel Δx should surpass a minimum value:

$$\Delta x_{min} = 2.3 \sqrt{\frac{D^3 [mm]}{g [mm]}}. \quad (34)$$

D is the diameter of a grain and g is the thickness of the sample. This means for a grain size of $10\mu\text{m}$ and a slab thickness of 10mm , the imaging resolution can reach $30\mu\text{m}$, whereas a larger grain size of $20\mu\text{m}$ and thinner samples of 1mm will drive the achievable imaging resolution toward $200\mu\text{m}$. The resolution limitations will be more drastic for performing tomographic reconstruction; in that case, the voxel dimension encompassing 10^4 grains will exceed the grain size, with a factor of 20 (at $D \approx 10\mu\text{m}$ voxel size becomes $\Delta x = 200\mu\text{m}$).

The polycrystalline simulation presented in Figure 8 assumed constant grain size within the material. Figure 10 presents neutron transmission simulations through a 1-cm-thick copper plate, using a log-normal distribution to represent the varying grain sizes that are typically found within engineered materials. Log-normal grain size distributions are commonly accepted to represent single-phase fully dense polycrystalline materials. They are parameterized⁴¹ by the mean (c) and standard deviation (b_{LN}). Neutron transmission simulations of polycrystalline materials with varying standard deviation (b_{LN}) for a log-normal distribution are presented in Figure 10. Equation B8 from Appendix B represents the current grain size value generated to follow the log-normal distribution; a relative standard deviation (c_v) of zero is consistent with a constant grain-size. Figure 10 presents the neutron transmission simulation of various c_v compared to that of a uniform distribution ($c_v=0$), as c_v increases, the distribution becomes broader, incorporating larger grains into the simulation. The influence of a broader

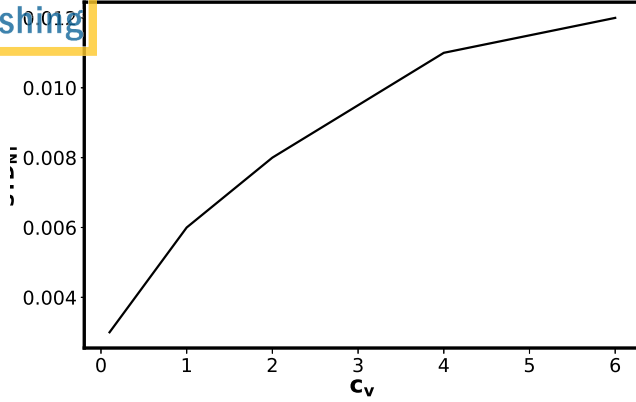


FIG. 11. The relationship of the standard deviation of the neutron transmission simulation (STD_{NT}) to the relative standard deviation of a log-normal distribution (c_v).

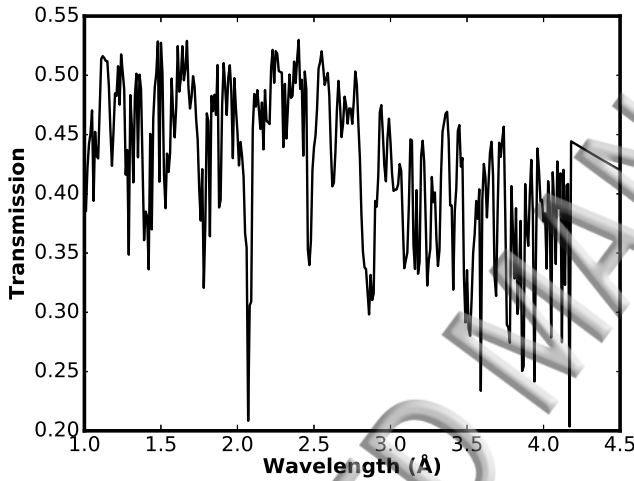


FIG. 12. As the relative standard deviation (c_v) of the log-normal grain size distribution increases, the grain size population will move toward larger grain sizes. The neutron transmission simulation spectra of a log-normal distribution with $b_{LN}=10$ resembles the neutron simulation spectra of a single crystal.

distribution of grain sizes on neutron transmission results in a higher level of 'noise', but the positions and heights of Bragg edges are preserved, suggesting that the mean grain size makes a good approximation. Figure 11 demonstrates the dependence of the standard deviation STD_{NT} of the neutron transmission simulation spectra on the relative standard deviation of the log-normal distribution, c_v . Note STD_{NT} is the standard deviation of the neutron transmission spectrum calculated for a log-normal distribution of grains relative to the reference spectrum corresponding to a constant grain-size. It also illustrates the effect of secondary extinction on the neutron transmission spectra as c_v increases. A c_v of 1 or less guarantees neutron transmission simulation will resemble that of a polycrystalline material. Ultimately a b_{LN} may be chosen that renders c_v to become very large

and leads to a log-normal grain-size distribution that contains grains that will be on the order of the voxel size, and thus the neutron transmission simulation will resemble the neutron simulation of a single crystal as shown in Figure 12.

C. A Comparison with Experimental Results

To provide a direct verification of simulation results for polycrystalline materials, neutron transmission for polycrystalline nickel (fcc) and iron (bcc) was calculated using the simulator and compared with experimental values. The experimental measurements were performed at the VULCAN^{25,26} beam-line at the SNS and the experimental technique is described in a separate publication⁴². Figure 13 is the comparison of the relative intensity ($1-T(\lambda)$) for Bragg edges obtained from experimentally measured spectra and calculated using the *sinpol* simulator for iron and nickel. The solid black line is the relative neutron intensity for nickel obtained via the experimental measurement, and the red dashed line is relative neutron intensity for nickel calculated with *sinpol*. The solid blue line is the relative neutron intensity for iron obtained via the experimental measurement, and the green dashed line is relative neutron intensity for iron calculated with *sinpol*. The main physical parameters required for neutron simulation calculations of Ni and Fe are shown in Table I. Figure 13 shows the comparison between experimental measurements and simulated neutron spectra. The calculations were performed for 2.42-mm-thick Ni plate segmented 500 times, with each segment consisting of a single column of 2420 distinct orientations; similarly calculations were performed for 3.12-mm-thick Fe plate segmented 375 times, with each segment consisting of a single column of 3120 distinct orientations. The lower part of Figure 13 shows the difference between the calculated and measured spectra. The errors in Bragg edge locations are expected to be slightly larger due to the uncertainty surrounding proper binning of wavelength to locate the Bragg edge. The main cause of differences in shape is likely due to *sinpol* using a Gaussian instrumental function to convolve with the intensity while the VULCAN instrument function is typically modelled with a convolution of two back-to-back exponentials to a pseudo-Voigt function⁴³.

IV. CONCLUSION

The *sinpol* library implements the presented neutron transmission calculations for single crystals as a function of crystal structure, neutron energy and crystal orientation. Simulations of a copper single crystal as a function of rotation were performed to study peak locations and intensity. Furthermore, the neutron transmissions through polycrystalline material were simulated by defining a distribution of crystal orientations. Polycrystalline neutron transmission of copper was verified with measurements found in the literature; simulation of Ni and Fe powder were verified

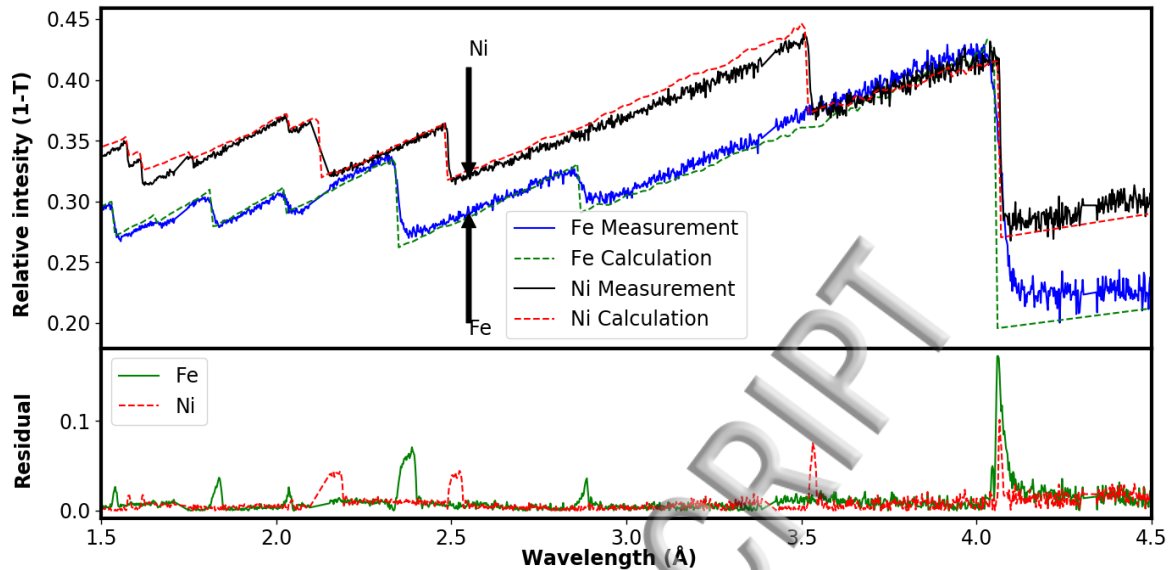


FIG. 13. Comparison of simulated neutron transmission of Fe and Ni to neutron transmission measurement of Fe and Ni.

with measurements made at ORNL. The number of grains in a grain distribution were varied to study the impact of grain-number statistics on Bragg edge visibility. A log-normal distribution was presented to study the impact of grain-size distribution on neutron transmission of a polycrystalline material. Effects of secondary extinction were observed on simulation of both single crystal neutron transmission and polycrystalline neutron transmission. The *sinpol* simulator can be used to illustrate the wavelength dependencies of transmission and cross section to help neutron experimental planning and data analysis. The model does not correspond solely to neutron Bragg edge transmission for polycrystalline with small random grains, it allows the analysis of wavelength-resolved neutron transmission for single crystal, oligocrystals, and is expected to impact the grain orientation mapping techniques⁴⁴.

The *sinpol* simulator presents the ability for the user to define angular distributions for neutron transmission calculations. Doing so allows for the simulation of a random distribution for powder materials. The ability for the user to define an angular distribution is quite useful, as it enables the user to input a probability density function to simulate texture for a polycrystalline sample; moreover a strain tensor can also be introduced to simulate three-dimensional strain. These capabilities are currently being tested and verified and will be included in following publications.

ACKNOWLEDGMENTS

Acknowledgements Research supported by the Geothermal Technologies Office, Office of Energy Efficiency and Renewable Energy, U.S. Department of Energy under contract DEAC05-00OR22725, Oak

Ridge National Laboratory, managed and operated by UT-Battelle, LLC.

The neutron transmission measurements were performed at the Spallation Neutron Source, a DOE Office of Science User Facility operated by the Oak Ridge National Laboratory. A.D.S. thanks the support from Laboratory Directed Research & Development project (LDRD-7886) at ORNL and gratefully acknowledges Dr. Hassina Bilheux for providing a state-of-the-art imaging detection system. We also thank Matthew Frost for the technical support and data reduction and Dr. An Ke for initiating these type of measurements at the VULCAN beamline.

Appendix A: Generation of Random Orientation

The symbol g represents the three parameters of rotation as a coordinates in Euler space. Furthermore, the Euler space is now a three dimensional periodic lattice with unit cell $2\pi, 2\pi, 2\pi$; however, the region is restricted by a glide plane and becomes asymmetric with unit cell $\{2\pi, \pi, 2\pi\}$, thus $\phi_1 \in \{0, 2\pi\}$, $\Phi \in \{0, \pi\}$, and $\phi_2 \in \{0, 2\pi\}$.

To generate a random distribution of orientations, we used the low-discrepancy multi-dimensional Halton³² sequence. The sequence is deterministic yet appear to be random for many purposes. In our case, a three dimensional sequence is used to generate a three dimensional array representing the orientation distribution. The array elements representing ϕ_1 and ϕ_2 are multiplied by 2π , while Φ is generated by taking the inverse cosine of twice the array element minus one.

The log-normal distribution for crystallites is parametrized by average value c and the standard deviation b on a logarithmic scale. According to Bucki and Kurzydowski⁴¹, the probability density for a number weighted log-normal grain volume distribution is given as

$$LN_N(v)dv = \frac{1}{vb\sqrt{2\pi}} \exp\left\{-\frac{1}{2}\left(\frac{\ln v - c}{b}\right)^2\right\} dv, \quad (B1)$$

where v is the volume.

The volume weighted log-normal distribution of the grain volume can be written as

$$LN_v(v)dv = \frac{1}{b\sqrt{2\pi}} \exp\left\{-\frac{1}{2}\left(\frac{\ln v - c}{b}\right)^2 - c - \frac{b^2}{2}\right\} dv. \quad (B2)$$

Let $v = \tau^3$ where τ is the thickness of a cubic grain; equation B3 is now expressed as function of the grain thickness τ

$$LN_v(\tau)d\tau = \frac{3\tau^2}{b\sqrt{2\pi}} \exp\left\{-\frac{1}{2}\left(\frac{\ln \tau - \frac{c}{3}}{\frac{b}{3}}\right)^2 - c - \frac{b^2}{2}\right\} d\tau. \quad (B3)$$

To create a cumulative grain-size distribution, we have to integrate equation B3

$$F(\tau) = \int_{-\infty}^{\ln \tau} \frac{3}{b\sqrt{2\pi}} \exp\left\{-\frac{1}{2}\left(\frac{y - \frac{c}{3}}{\frac{b}{3}}\right)^2 - c - \frac{b^2}{2}\right\} e^{3y} dy \quad (B4)$$

$$= \frac{1}{2} + \frac{1}{2} \operatorname{erf}\left(\frac{\ln \tau - \frac{c}{3} - \frac{b^2}{2}}{\sqrt{2}\frac{b}{3}}\right). \quad (B5)$$

Following Bucki and Kurzydowski⁴¹, the volume weighted coefficient of variation (relative std.) for the log-normal distribution is given as

$$c_v^2 = e^{b^2} - 1, \quad (B6)$$

and the volume weighted mean volume

$$E_v = \tau_v^3 = \exp\left(c - \frac{3b^2}{2}\right). \quad (B7)$$

To generate a volume weighted log-normal distributed grain thickness, equation B5 is solved for a random number $y_o \in \{0, 1\}$

$$\tau = \tau_v \left((1 + c_v)^{-\frac{1}{6}} \right) \exp\left[\frac{\sqrt{2\ln(1 + c_v)}}{3} \operatorname{erf}^{-1}(2y_o - 1) \right]. \quad (B8)$$

In the above calculations, the use of volume weighted distribution is appropriate for a column simulation. For multiple rays interacting with multiple columns, an area-weighted distribution should be considered instead of a volume-weighted distribution.

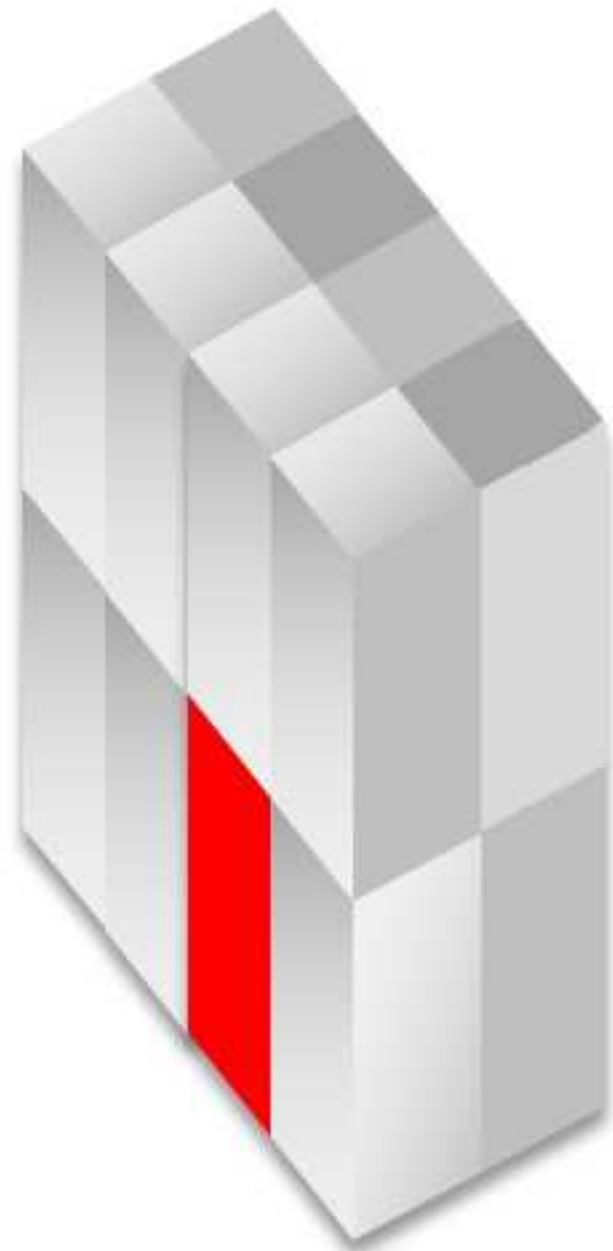
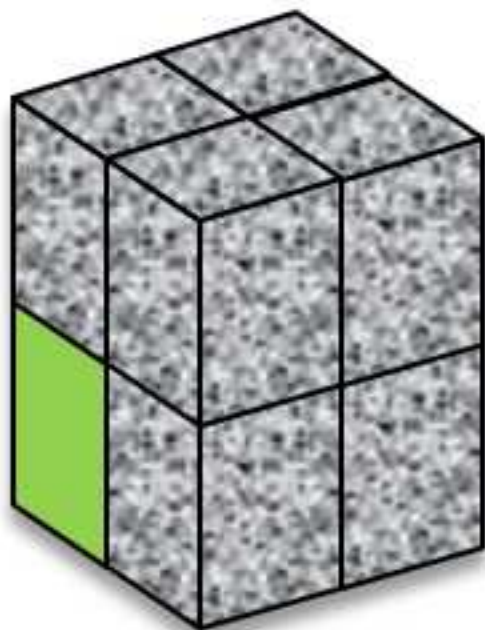
The program, which we call *sinpol*, is written in Python programming language and has been packaged into a new flexible neutron transmission library. The python package allows for easy installation and use on multiple platforms (e.g. Linux, MacOSX, Windows), which in turn extends the availability of the library. For this work, neutron transmission calculations were performed on a 2.50 GHz intel core i5 processor personal laptop. The calculation time for 10 distinct orientations is less than a second, and the calculation time for 10,000 distinct orientations is 400 seconds. The time scales linearly with the number of distinct orientations used for the transmission calculation. The simulations for 10-million orientations were calculated with a cluster; the code was easily parallelized by sending 10,000 orientations to each node. On personal computers, the code can be parallelized via multiprocessing processes. Parallelization for using gpus via pyCuda is another possible solution for higher speeds.

Currently *sinpol* calculates one neutron transmission spectrum for a voxel. To simulate an image of multiple voxels, it is necessary to calculate each voxel separately, and a parallel ray tracer can then be used to simulate the final image. Furthermore for computed tomography, the sample can be rotated by the angle ρ to obtain the neutron transmission spectrum for a voxel rotated by the angle ρ ; similarly a parallel ray tracer can be used to simulate a final image.

- ¹D. Mitchell and P. Powers, Physical Review **50**, 486 (1936).
- ²O. Halpern, M. Hamermesh, and M. Johnson, Physical Review **59**, 981 (1940).
- ³E. Fermi, W. Sturm, and R. G. Sachs, Physical Review **71**, 589 (1947).
- ⁴J. Carpenter and C. Loong, *Elements of Slow-Neutron Scattering* (Cambridge University Press, Cambridge, UK, 2015).
- ⁵K. Meggers, H. G. Priesmeyer, W. Trela, C. Bowman, and M. Dahms, Nuclear Instrument Method B **88**, 423 (1994).
- ⁶S. Vogel, *A Rietveld-Approach for the Analysis of Neutron Time-Of-Flight Transmission Data.*, Ph.D. thesis, Christian-Albrecht- Univ. Kiel (2000).
- ⁷J. Santisteban, Journal of Applied Crystallography **38**, 934 (2005).
- ⁸J. Santisteban, L. Edwards, A. Steuwer, and P. Withers, Journal of Applied Crystallography **34**, 289 (2001).
- ⁹I. S. Anderson, R. L. McGreevy, and H. Z. Bilheux, *Neutron Imaging and Applications. Neutron Scattering Applications and Techniques* (Springer, Boston, Ma, 2009).
- ¹⁰A. Steuwer, P. Withers, J. Santisteban, and L. Edwards, Journal of Applied Physics **97** (2005).
- ¹¹B. Abbey, Y. Zhang, W. Vorster, and A. Korsunsky, Procedia Engineering **1**, 185 (2009).
- ¹²N. Kardjilov, A. Hilger, I. Manke, M. Strobl, M. Dawson, and J. Banhart, Nuclear Instrument Method A **605**, 13 (2009).
- ¹³A. S. Tremsin, J. B. McPhate, A. Steuwer, W. Kockelmann, A. M. Paradowska, J. F. Kelleher, J. V. Vallega, O. H. W. Siegmund, and W. B. Feller, Strain **48**, 296 (2012).
- ¹⁴R. Woracek, D. Penumadu, N. Kardjilov, A. Hilger, M. Boin, J. Banhart, and I. Manke, Adv. Mater. **26**, 4069 (2014).
- ¹⁵M. Adib, N. Habib, I. Bashter, H. Morcos, M. Fathallah, and M. E.-M. abs A.Saleh, Annals of Nuclear Energy **60**, 163 (2013).
- ¹⁶K. Naguib and M. Adib, Phys. Rev. **29**, 1441 (1996).
- ¹⁷G. Bacon and R. Lowde, Acta Crys. **1**, 303 (1948).
- ¹⁸O. Dietrich and L. A. Nielsen, Acta Cryst. **18**, 184 (1965).

- ¹⁹V. Sears, *Acta Cryst.* **A53**, 35 (1997).
- ²⁰M. Boin, *Journal of Applied Crystallography* **45**, 603 (2012).
- ²¹H. Spine, *Acta Crystallographica* **A44**, 374 (1988).
- ²²T. S. Rime, *Acta Crystallographica* **38**, 507 (1985).
- ²³H. Sato, T. Kamiyama, and Y. Kiyonagi, *Materials Transactions* **52**, 1294 (2011).
- ²⁴F. Malamud and J. Santisteban, *Journal of Applied Crystallography* **49**, 348 (2016).
- ²⁵X.-L. Wang and A. D. Stoica, *Nuclear Instrument and Methods A* **600**, 309 (2009).
- ²⁶K. An, H. D. Skorpenske, A. D. Stoica, and et al., *Metallurgical and Materials Transactions A* **42A**, 95 (2011).
- ²⁷R. Woracek, J. Santisteban, A. Fedrigo, and M. Strobl, *Nuclear Inst. and Methods in Physics Research A* **878**, 141 (2018).
- ²⁸R. W. Grosse-Kunstleve, *Acta Cryst* **A55**, 383 (1999).
- ²⁹A. Larsen, J. Mortensen, J. Blomqvist, I. Castelli, R. Christensen, M. Dulak, J. Friis, M. Groves, B. Hammer, C. Hargus, E. Hermes, P. Jennings, P. Jensen, J. Kermode, J. Kitchin, E. Kolsbjerg, J. Kubal, and et al., *Journal of Physics: Condensed Matter* **29**, 273002 (2017).
- ³⁰V. Sears, *Neutron News* **3**, 29 (1992).
- ³¹H. J. Bunge, *Texture Analysis in Materials Science*. (London:Butterworths, 1982).
- ³²J. Halton, *Numerische Mathematik* **2**, 84 (1960).
- ³³N. Popa, *Journal of Applied Crystallography* **33**, 103 (2000).
- ³⁴W. H. Zachariasen, *Theory of X-ray Diffraction in Crystals* (New York: Wiley, 1975).
- ³⁵G. E. Bacon, *Neutron Diffraction 3rd edn.* (Oxford:Clarendon, 1975).
- ³⁶A. Freund, *Nucl. Instrum. Methods* **213**, 495 (1983).
- ³⁷M. Renninger, *Z. Phys* **106**, 141 (1937).
- ³⁸R. Moon and C. Shull, *Acta Crystallogr.* **17**, 805 (1964).
- ³⁹E. Rossmanith, *Journal of Applied Crystallography* **33**, 921 (2000).
- ⁴⁰W. Kockelmann, G. Frei, E. Lehmann, P. Vontobel, and J. Santisteban, *Nuclear Instrument and Methods in Physics Research A* **578**, 421 (2007).
- ⁴¹J. Bucki and K.J. Kurzydowski, *Scripta Metall* **28**, 689 (1993).
- ⁴²G. Song, J. Y. Y. Lin, J. C. Bilheux, Q. Xie, K. An, A. D. Stoica, M. M. Kirka, R. R. Dehoff, S. N. Dryepondt, A. Tremsin, L. J. Santodonato, and H. Bilheux, *Journal Imaging* **3**, 65 (2017).
- ⁴³A. Larson and R. V. Dreele, *General structure analysis (GSAS) LAUR 86-748 Los Alamos National Laboratory Report* (2004).
- ⁴⁴H. Sato, Y. Shiota, S. Morooka, Y. Todaka, N. Adachi, S. Sadamastu, K. Oikawa, M. Harada, S. Zhang, Y. Su, T. Kamiyama, M. Ohnuma, M. Furusak, T. Shinohara, and Y. Kiyonagi, *Journal of Applied Crystallography* **50**, 1601 (2017).

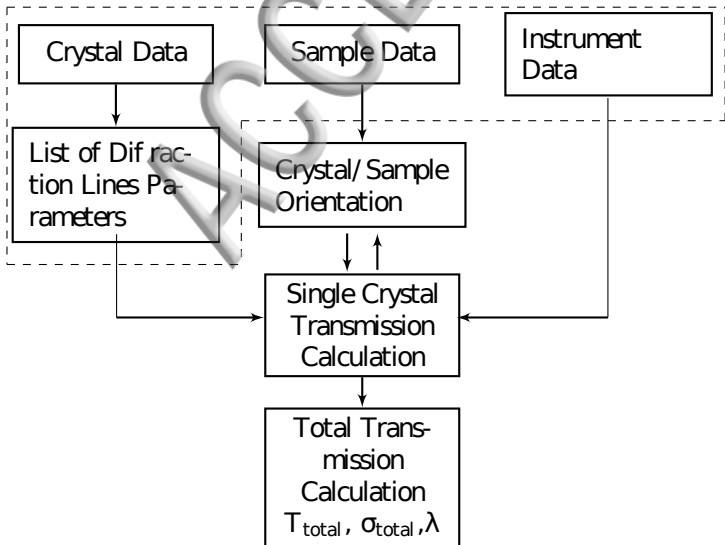
ACCEPTED MANUSCRIPT

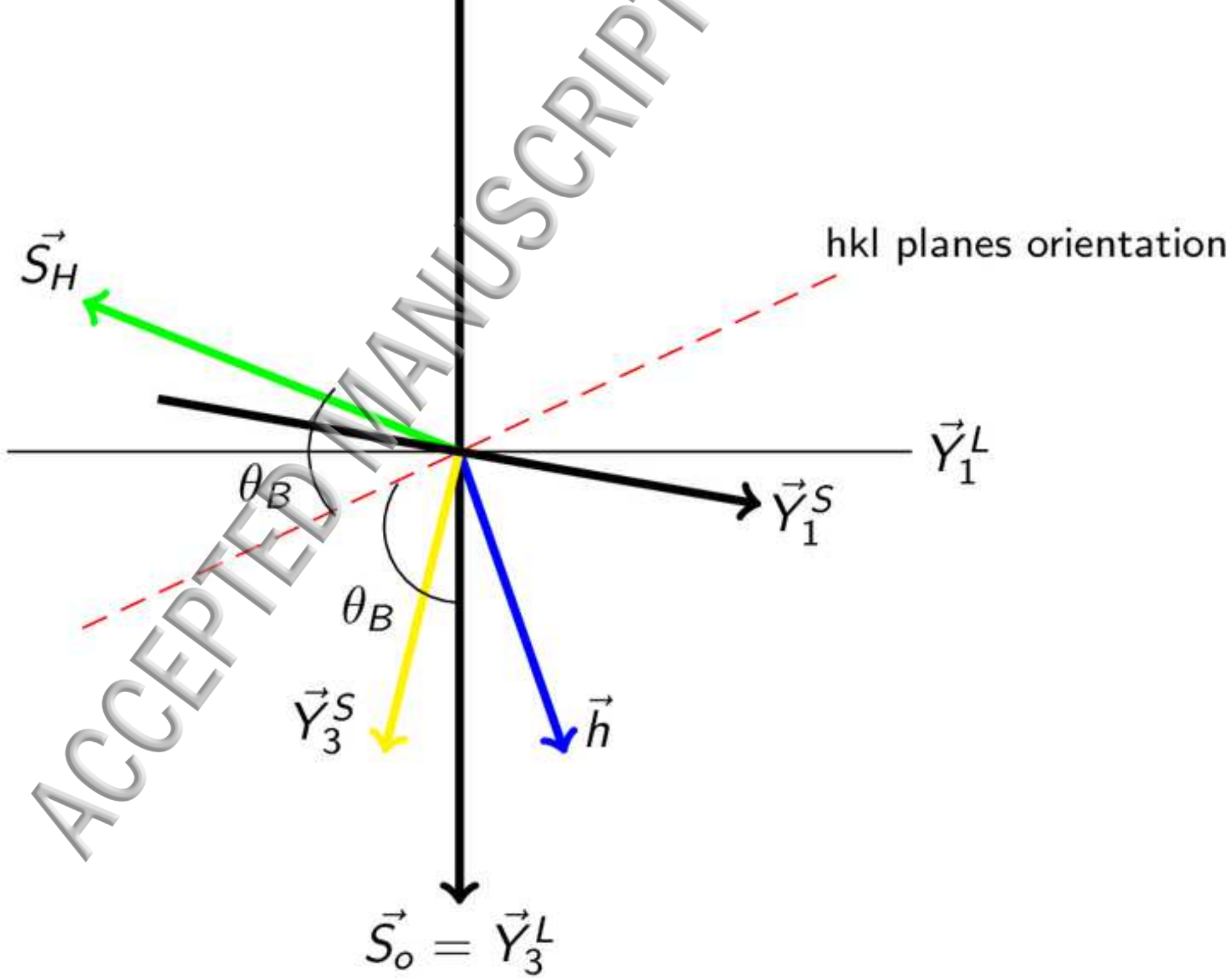


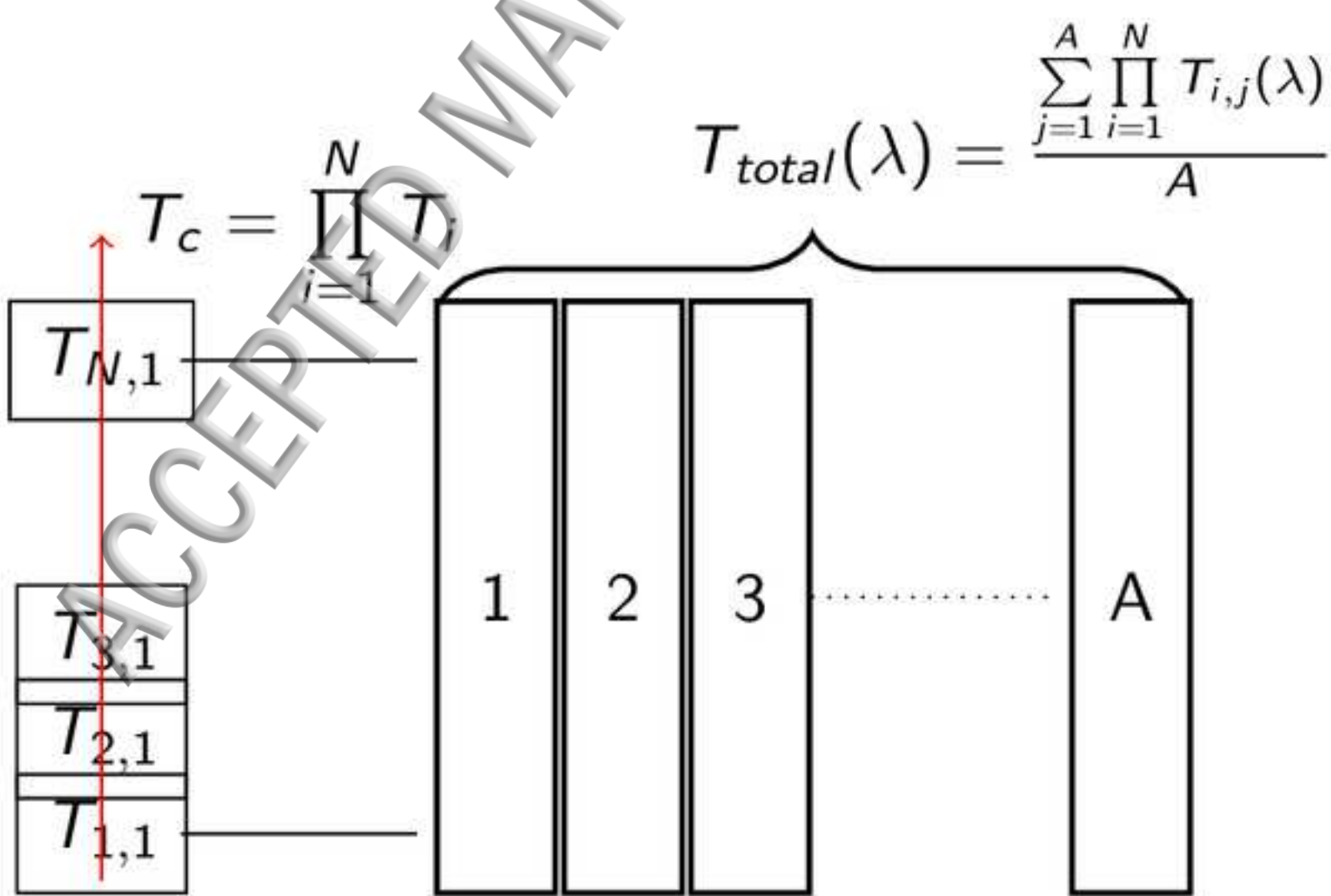
Grain

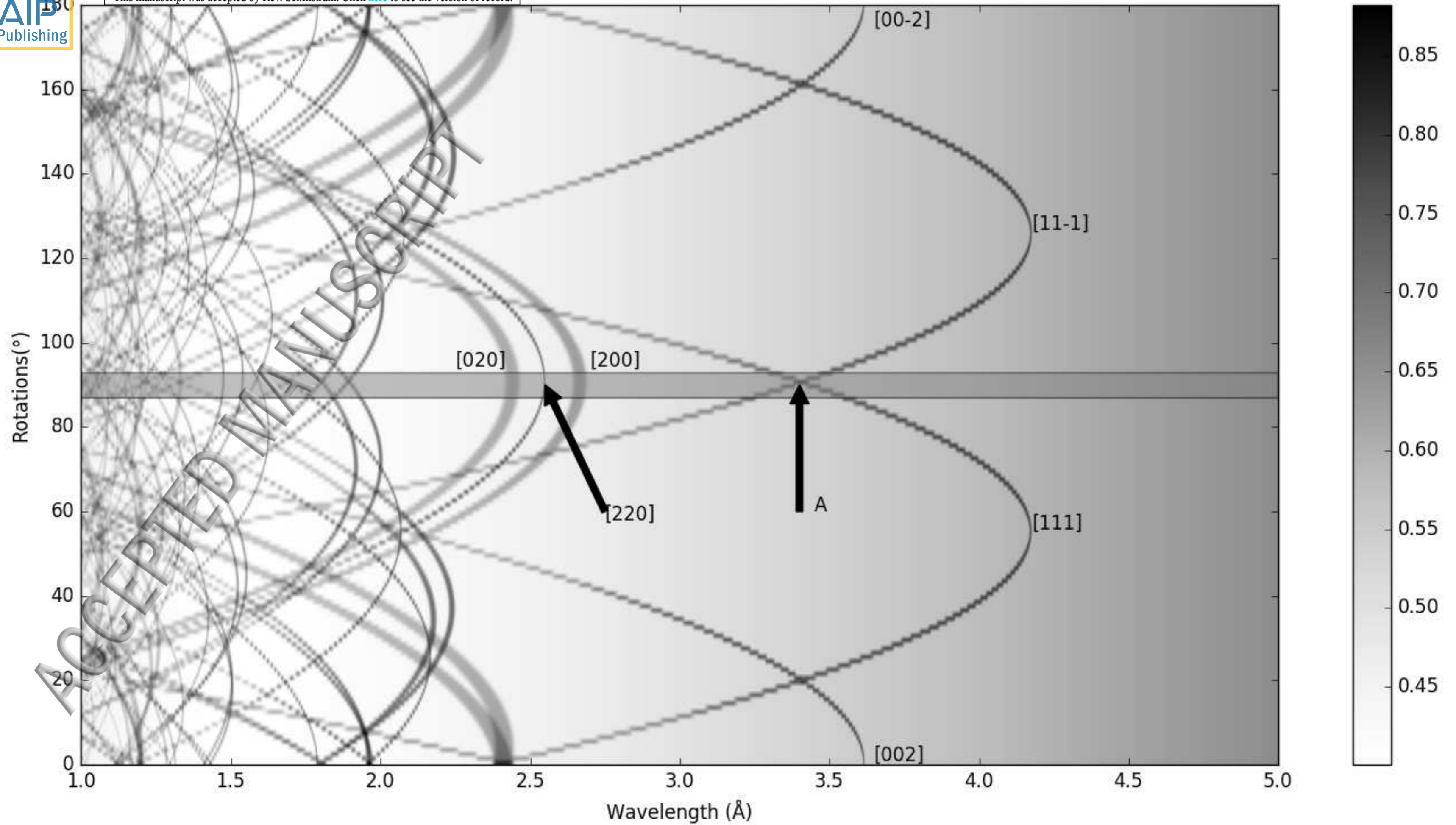
Voxel

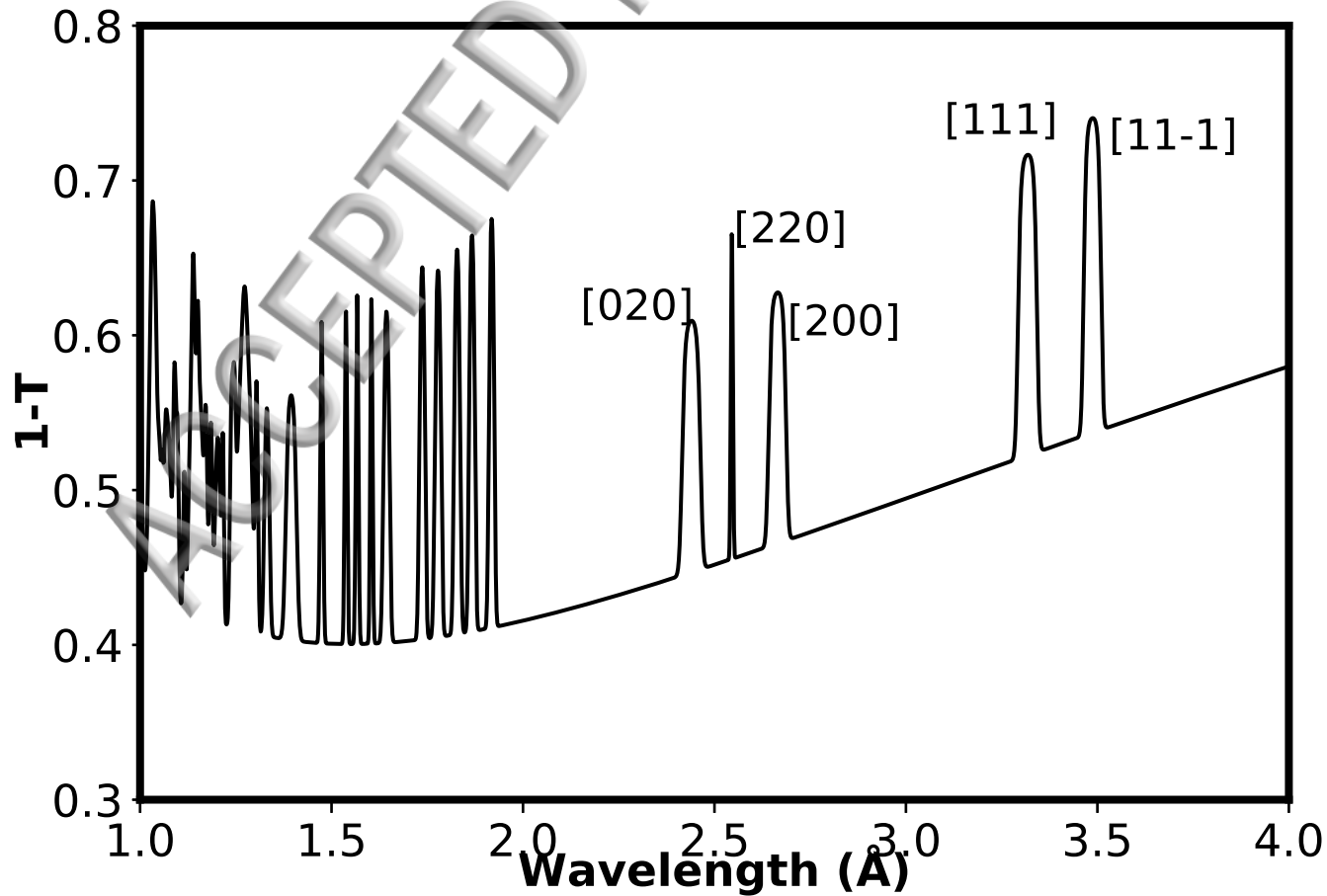
Sample

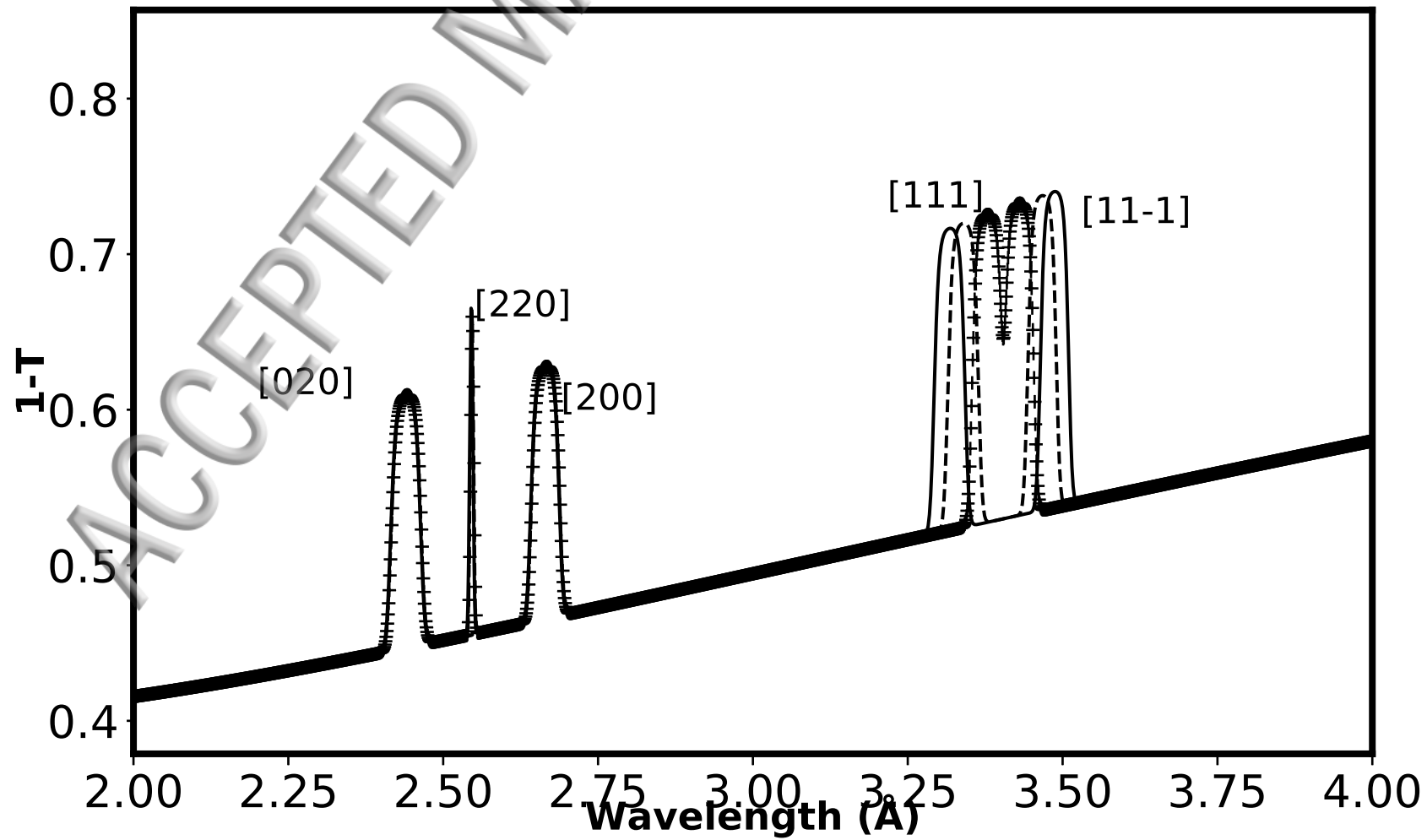


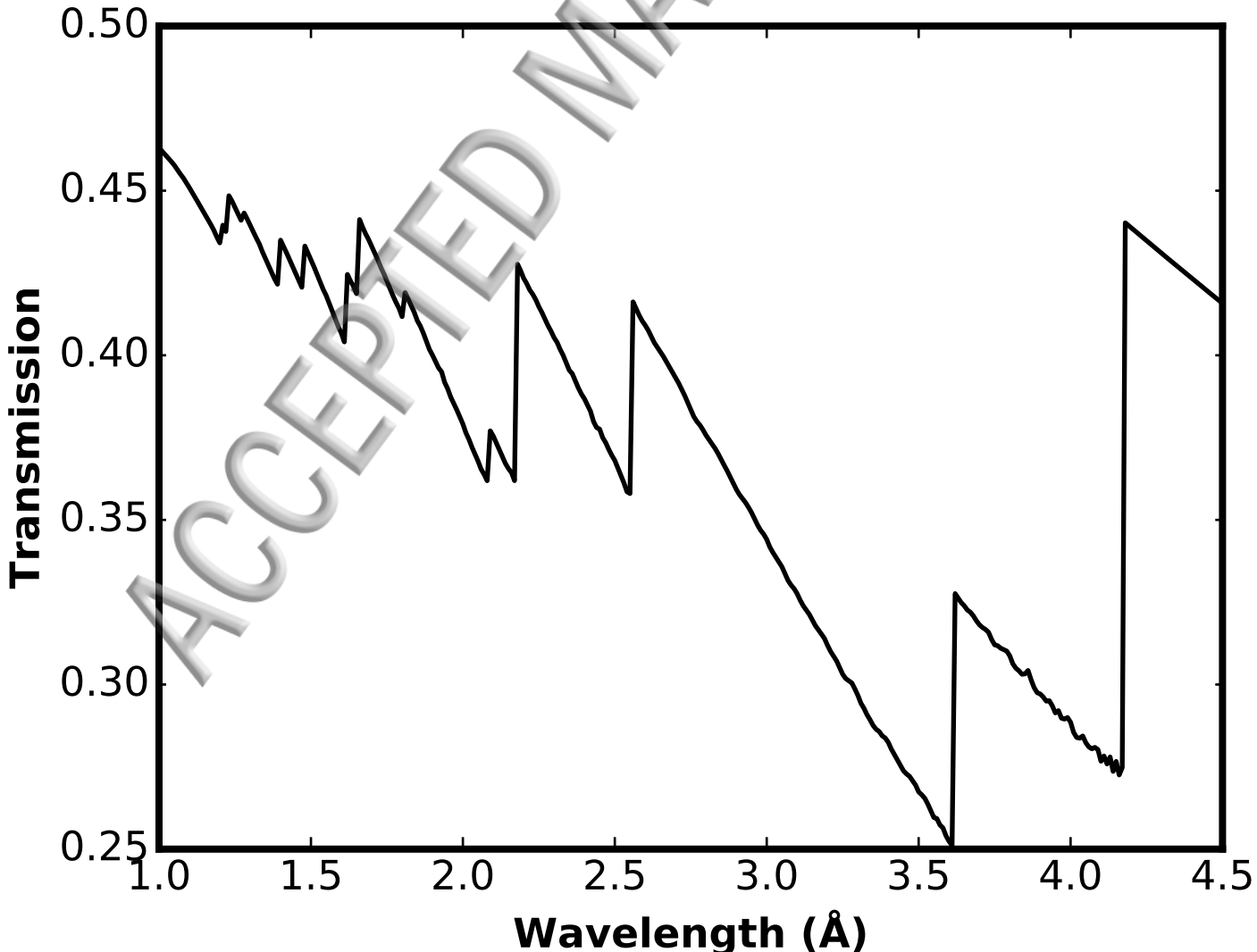


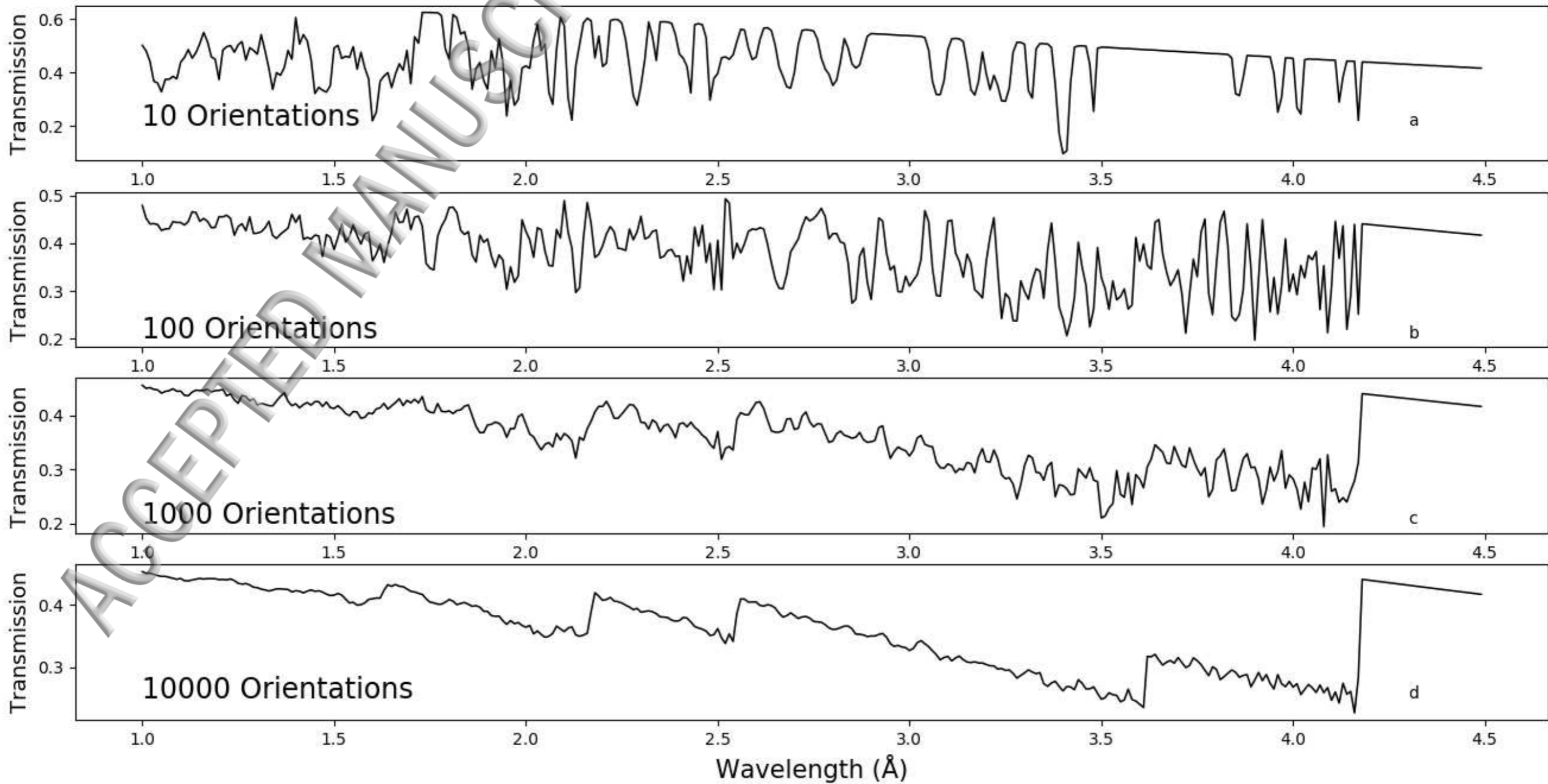


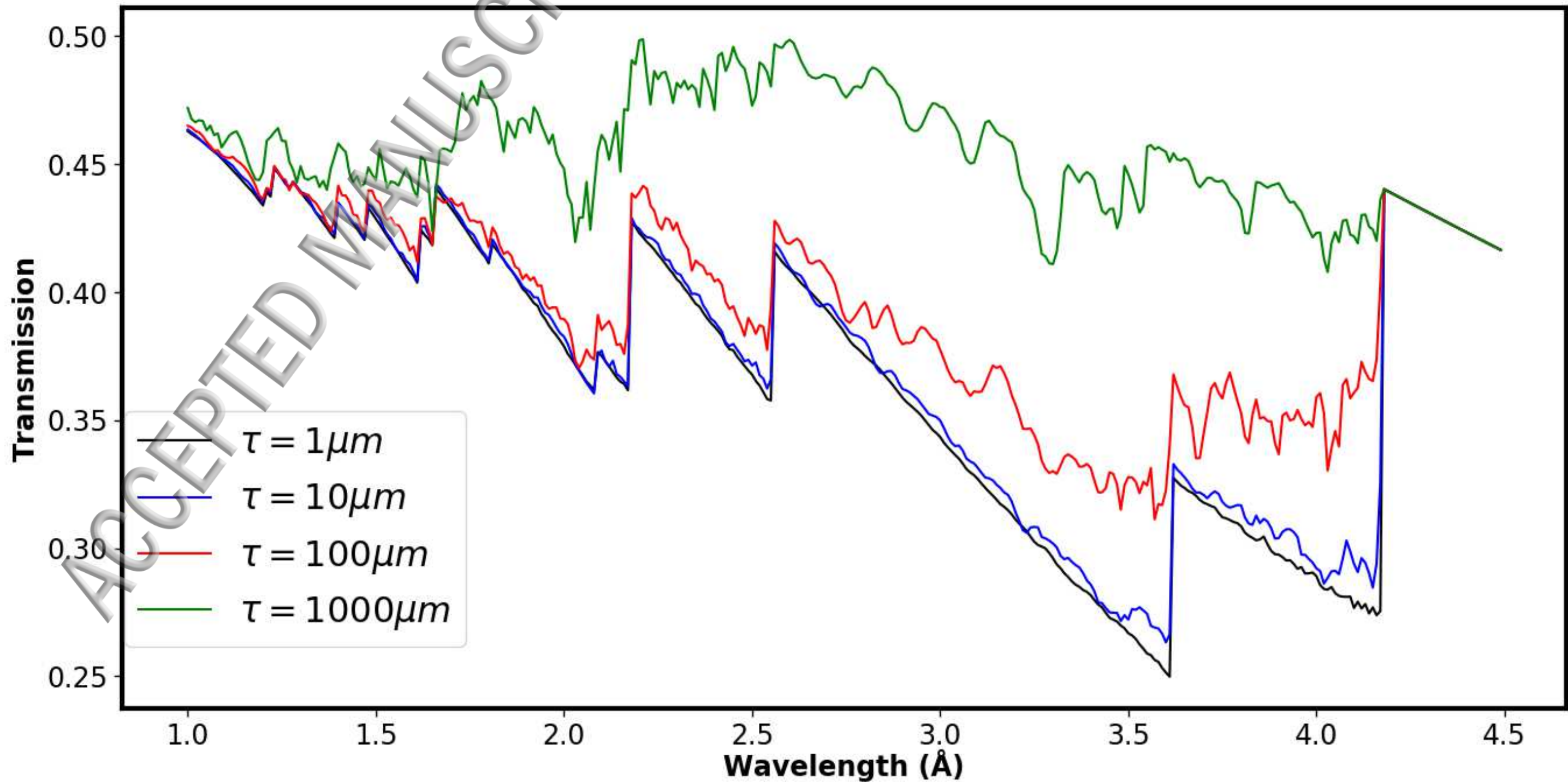


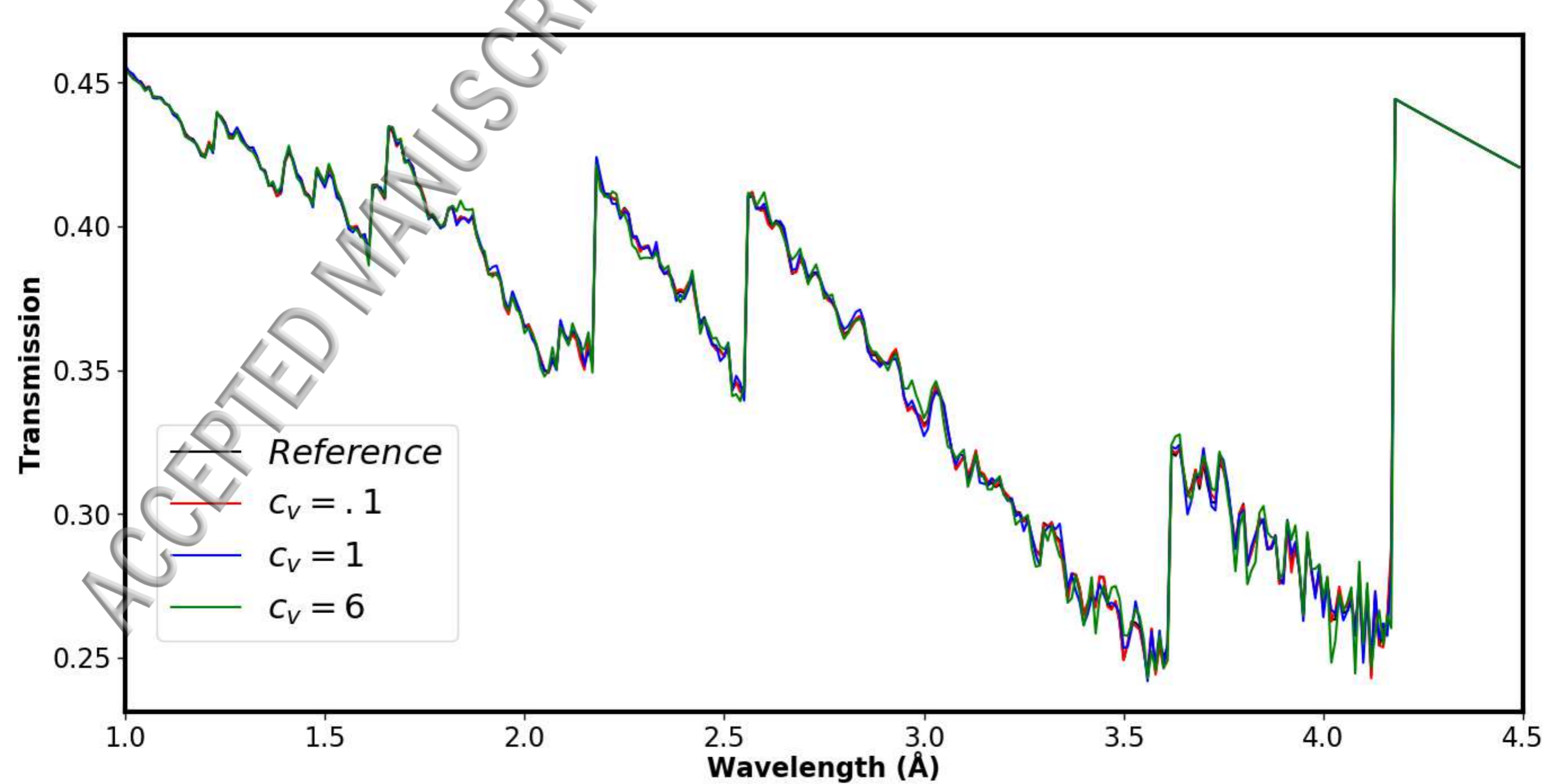












ACCEPTED MANUSCRIPT

